Comparison of stabilization strategies applied to scale-resolved simulations using the discontinuous Galerkin Method

Amaury Bilocq, Maxime Borbouse, Nayan Levaux, Vincent E. Terrapon, Koen Hillewaert[a]

[a] *Department of Aerospace and Mechanical Engineering, Université de Liège, Allée de la Découverte 9, Liège, 4000, , Belgium*

Abstract

This study evaluates several stabilization strategies for the discontinuous Galerkin Spectral Element Method in scale-resolved simulations of compressible turbulence, with emphasis on accuracy, robustness, and computational efficiency. A novel selective entropy-stable approach (DG-ES) is introduced, which activates entropy stabilization only in localized regions to enhance robustness while minimizing dissipation. The performance of DG-ES is benchmarked against artificial viscosity (DG-AV), as well as fully entropy-stable methods based on Gauss–Legendre (ESDG-GL) and Gauss–Lobatto (ESDG-GLL) quadratures, across a range of canonical shock–turbulence interaction test cases. Results show that DG-AV performs well in scenarios involving highly mobile shocks, effectively resolving both shocks and small-scale turbulence, but its accuracy deteriorates in stationary shock configurations. Additionally, DG-AV is highly sensitive to the choice and calibration of its detector. In contrast, entropy-stable methods improve post-shock turbulence accuracy but tend to introduce spurious oscillations near shocks and incur greater computational cost. The ESDG-GL method suffers from entropy projection errors in shocklet-dominated regions, while ESDG-GLL is affected by excess dissipation due to under-integration. DG-ES achieves a favorable balance, accurately capturing turbulence with reduced sensitivity to detector calibration and maintaining competitive efficiency. However, like the ESDG-GL, it requires smaller time steps to ensure stability in the presence of strong shocks, due to the stiffness introduced by the entropy projection.

Keywords: Discontinuous Galerkin, Discontinuous Galerkin Spectral Element Method, Entropy Stability, Budget Kinetic Energy, Turbulence, Transonic Flows, Artificial Viscosity

1. Introduction

In recent years, the discontinuous Galerkin (DG) method has gained significant interest in the field of computational fluid dynamics (CFD) due to its high-order accuracy, flexibility in handling complex geometries, and excellent parallel scalability [1, 2, 3]. The

Email address: amaury.bilocq@uliege.be ()

method has demonstrated rapid convergence and accuracy in the context of Direct Numerical Simulation (DNS) and Large-Eddy Simulation (LES) of aeronautic applications by accurately detecting the laminar-to-turbulent transition and correctly representing turbulence in the subsonic regime on either airfoils [4, 5, 6] or turbomachinery passages [7].

However, aeronautic applications often operate under conditions where the flow becomes transonic, leading to complex interactions between shock waves, turbulence, and boundary layers. In particular in the novel high-speed low-pressure compressors and turbines [8, 9], featuring transitional flow at high Mach numbers, DNS and LES are becoming increasingly important from an industrial perspective. These interactions pose significant challenges for numerical methods, which often struggle to maintain accuracy and stability in such conditions [10, 11]. Moreover, DNS is rarely feasible for many industrial flows due to the relatively high Reynolds numbers involved, which necessitate extremely fine spatial and temporal resolutions. Instead, LES is employed, where only the larger turbulent structures are resolved. This approach results in highly under-resolved turbulence, further complicating the simulations [12, 13].

Stabilization techniques are employed to ensure numerical stability, but these techniques should have the smallest possible impact on the overall accuracy of the simulation. Importantly, stabilization is generally not required throughout the entire domain but should be selectively applied wherever shocks or under-resolved turbulent features are present. In the non-troubled regions, the numerical scheme must maintain high accuracy to capture the intricate details of the turbulent flow.

To address these challenges, various stabilization techniques have been proposed in the context of the DG method. Artificial viscosity methods introduce additional dissipation to stabilize the solution and accurately capture shocks but can be overly diffusive [14] introducing large error on the turbulence budgets. These methods range from simple Laplacian-based approaches [15] to more sophisticated physics-based strategies [16] that adaptively adjust the viscosity based on local flow conditions, such as dilatation and vorticity. Entropy-stable schemes [17, 18] ensure that the numerical solution adheres to the second law of thermodynamics, enhancing robustness and stability but at the cost of computational efficiency [19]. So far, the literature has not really acknowledged nor quantified the significant, yet counter-intuitive impact that these methods have at the non-linear level, in particular concerning small flow features.

In this work, we aim to evaluate the performance of different DG-based stabilization techniques, including artificial viscosity (DG-AV) and entropy stability based on either the Gauss-Lobatto quadrature (ESDG-GLL) [17, 20, 19] or the Gauss-Legendre quadrature using the hybridized SBP operator (ESDG-GL) [21, 22, 18, 23], in simulating under-resolved compressible turbulent flows. We compare these methods with the vanilla DG method to assess their impact on accuracy, robustness, and computational cost. Furthermore, we propose an alternative stabilization approach that maintains the accuracy of the DG method while ensuring robustness at an affordable computational cost by applying entropy stability only locally and not globally (DG-ES). To assess the convergence of the methods, we use the budget of kinetic energy [24]. The kinetic energy equation provides a comprehensive measure of the energy variation and dissipation processes within the flow. It has been observed that entropy stable methods, despite not adding explicit diffusion, significantly impact these budgets and should therefore be used with caution.

The structure of the paper is as follows: Section 2 briefly introduces the compressible Navier-Stokes equations, the global entropy inequality, and the budget of kinetic energy used to study the convergence of the simulations. Section 3 reviews the numerical methods employed to discretize the compressible Navier-Stokes equations, from the vanilla DG to the entropy stable schemes. Section 4 presents and discusses the numerical results, including the accuracy, robustness, and computational cost of the methods on four under-resolved compressible turbulent cases: compressible homogeneous turbulence, the compressible Taylor-Green vortex, the strong-vortex/shock-wave interaction and shock-turbulence interaction. The impact of the detectors on the stabilization methods is also presented. We finally summarize the main findings in Section 5.

2. Compressible Navier-Stokes equations

The governing equations used in this work are the compressible Navier-Stokes equations. Let $\boldsymbol{u}$ denote the vector of conservative variables

$$\boldsymbol{u} = \{\rho, \rho\boldsymbol{v}, \rho E\},$$

where ρ is the density, $\boldsymbol{v}$ the velocity vector, E the specific total energy and H total enthalpy, defined as

$$E = e + k, \quad H = h + k = e + \frac{p}{\rho} + k,$$

e being the internal energy, h the enthalpy and $k = \boldsymbol{v} \cdot \boldsymbol{v}/2$ the kinetic energy. The relationships between pressure p, density ρ, temperature T, energy e and enthalpy h are defined by the following constitutive equations

$$p = \rho e(\gamma - 1) = \rho RT, \quad e = c_v T, \quad h = c_v T + \frac{p}{\rho} = c_p T,$$

where γ is the specific heat ratio, R is the gas constant and c_v and $c_p = c_v + R$ are the specific heat capacities at constant volume and pressure, respectively. As suggested by the constitutive equations, all these parameters will be considered constant throughout the development in this paper.

The compressible Navier-Stokes equations can be written in the following form

$$\frac{\partial \boldsymbol{u}}{\partial t} + \nabla \cdot \boldsymbol{f}(\boldsymbol{u}) = \nabla \cdot \boldsymbol{d}(\boldsymbol{u}, \nabla \boldsymbol{u}). \tag{1}$$

Here the convective flux $\boldsymbol{f}$ and the diffusive flux $\boldsymbol{d}$ vectors are given by

$$\boldsymbol{f} = \begin{pmatrix} \rho\boldsymbol{v} \\ \rho\boldsymbol{v} \cdot \boldsymbol{v} + p\mathbf{I} \\ \rho\boldsymbol{v} \cdot H \end{pmatrix} = \begin{pmatrix} \rho v_i \\ \rho v_i v_1 + p\delta_{i1} \\ \rho v_i v_2 + p\delta_{i2} \\ \rho v_i v_3 + p\delta_{i3} \\ \rho v_i H \end{pmatrix} \boldsymbol{e}_i, \quad \boldsymbol{d} = \begin{pmatrix} 0 \\ \boldsymbol{\tau} \\ \boldsymbol{\tau} \cdot \boldsymbol{v} + \boldsymbol{Q} \end{pmatrix} = \begin{pmatrix} 0 \\ \tau_{1i} \\ \tau_{2i} \\ \tau_{3i} \\ v_j \tau_{ji} + Q_i \end{pmatrix} \boldsymbol{e}_i,$$

where $\boldsymbol{e}_i$ is the unit vector in direction i and Einstein notation is used. The heat flux vector is defined as $\boldsymbol{Q} = \kappa \nabla T$, where κ is the thermal conductivity. For a Newtonian fluid, the shear stress tensor $\boldsymbol{\tau}$ is expressed as

$$\boldsymbol{\tau} = 2\mu \boldsymbol{S}^{\mathrm{d}} + \zeta \left(\nabla \cdot \boldsymbol{v}\right) \mathbf{I}$$

where $\boldsymbol{S}^{\mathrm{d}} = \mathbf{S} - \frac{1}{3}(\nabla \cdot \boldsymbol{v})\,\mathbf{I}$ is the shear rate tensor, $\boldsymbol{S} = \frac{1}{2}\left(\nabla \boldsymbol{u} + \nabla \boldsymbol{u}^T\right)$ is the strain rate tensor, μ is the dynamic viscosity and the bulk viscosity ζ is set to $\zeta = 0$, following Stokes hypothesis. The stress tensor can be rewritten as

$$\boldsymbol{\tau} = \mu\left(\nabla \boldsymbol{u} + \nabla \boldsymbol{u}^T\right) - \frac{2\mu}{3}(\nabla \cdot \boldsymbol{v})\,\mathbf{I}.$$

2.1. Kinetic energy balance

The kinetic energy balance equation, derived from the mass and momentum conservation laws, for a domain Ω with boundaries $\partial\Omega$ is expressed as

$$-\frac{\mathrm{d}}{\mathrm{d}t}\int_\Omega \rho k \,\mathrm{d}V = \int_\Omega \boldsymbol{\tau} : \nabla \boldsymbol{v} \,\mathrm{d}V - \int_\Omega p \nabla \cdot \boldsymbol{v} \,\mathrm{d}V + \int_{\partial\Omega} (p\boldsymbol{v} - \boldsymbol{\tau} \cdot \boldsymbol{v} - \rho k \boldsymbol{v}) \cdot \mathbf{n} \,\mathrm{d}S, \quad (2)$$

where $\mathbf{n}$ is the outward normal vector on the boundary $\partial\Omega$. The left-hand side of equation (2) represents the rate of change of kinetic energy, while the right-hand side accounts for the dissipation of kinetic energy due to viscous effects, the work done by pressure forces, and the transport of kinetic energy across the domain boundaries.

By following the formulations of Zeman [25] and Sarkar [26] for Newtonian fluids, the viscous dissipation rate can be decomposed as

$$\int_\Omega \boldsymbol{\tau} : \nabla \boldsymbol{v} \,\mathrm{d}V = \int_\Omega \mu\,(\boldsymbol{\omega} \cdot \boldsymbol{\omega}) \,\mathrm{d}V + \frac{4}{3}\int_\Omega \mu (\nabla \cdot \boldsymbol{v})^2 \,\mathrm{d}V, \quad (3)$$

where $\boldsymbol{\omega} = \nabla \times \boldsymbol{v}$ is the vorticity. The kinetic energy dissipation rate is therefore the sum of three contributions:

$$\underbrace{-\frac{\mathrm{d}}{\mathrm{d}t}\int_\Omega \rho k \,\mathrm{d}V}_{\epsilon_1} = \underbrace{2\int_\Omega \mu \xi \,\mathrm{d}V}_{\epsilon_2} \underbrace{+\frac{4}{3}\int_\Omega \mu (\nabla \cdot \boldsymbol{v})^2 \,\mathrm{d}V}_{\epsilon_3} \underbrace{-\int_\Omega p \nabla \cdot \boldsymbol{v} \,\mathrm{d}V}_{\epsilon_4} \underbrace{+\int_{\partial\Omega} (p\boldsymbol{v} - \boldsymbol{\tau} \cdot \boldsymbol{v} - \rho k \boldsymbol{v}) \cdot \mathbf{n} \,\mathrm{d}S}_{\epsilon_5}, \quad (4)$$

where $\xi = \boldsymbol{\omega} \cdot \boldsymbol{\omega}/2$ denotes the enstrophy. The second term, ϵ_2, represents the solenoidal contribution to the viscous dissipation rate in compressible turbulence [25, 26, 2, 27]. Since high-enstrophy regions are associated with small-scale vortical structures, the solenoidal dissipation rate is a measure of the dissipation of kinetic energy into heat due to the presence of small-scale vortices.

The third term, ϵ_3, corresponds to the dilatational contribution to the viscous dissipation rate, representing the portion of kinetic energy dissipation associated with compressive or expansive motions. This contribution becomes particularly significant in flows with strong compressibility effects, such as high-speed, shock-dominated, or acoustically active regimes.

The fourth term, ϵ_4, represents the work done by pressure forces and describes the energy transfer resulting from pressure acting on volumetric changes within the flow. This term is closely linked to compressibility effects, such as shock waves, expansion fans, and acoustic phenomena. Positive values indicate the dissipation of kinetic energy

through an increase in internal energy, as seen in shock waves. Conversely, negative values reflect an increase in kinetic energy due to a decrease in internal energy, as occurs in expansion fans.

The fifth term, ϵ_5, represents the net flux of kinetic energy across the boundaries of the domain. It comprises three physical mechanisms: the work done by pressure forces, the mechanical work associated with viscous stresses, and the convective transport of kinetic energy.

The difference between the right and left-hand-side is the budget of kinetic energy, defined as $\Delta\epsilon = \epsilon_2 + \epsilon_3 + \epsilon_4 + \epsilon_5 - \epsilon_1$. Since this balance is only approximately satisfied by the discretized equations of Section 3, it may be used as a direct indicator of the *instantaneous* numerical error.

2.2. Entropy variables

Let U denote a convex entropy function [28] of equation (1). The only admissible entropy function for the compressible Navier-Stokes equations with non-zero heat flux is (a multiple of) [29]

$$U(\boldsymbol{u}) = -\rho s, \tag{5}$$

where $s = \log\left(\frac{p/p_{\text{ref}}}{(\rho/\rho_{\text{ref}})^\gamma}\right)$ is the nondimensional *physical* entropy [29]. The entropy variables $\boldsymbol{w}(\boldsymbol{u})$ are defined as the Jacobian of the *mathematical* entropy function with respect to the conservative variables

$$\boldsymbol{w}(\boldsymbol{u}) = \frac{\partial U}{\partial \boldsymbol{u}}. \tag{6}$$

One of the conditions for U to be a mathematical entropy function is the existence of a scalar flux function $\boldsymbol{\mathcal{F}}$, called the entropy flux, for which

$$\frac{\partial \boldsymbol{\mathcal{F}}}{\partial \boldsymbol{u}} = \frac{\partial U}{\partial \boldsymbol{u}} \frac{\partial \boldsymbol{f}}{\partial \boldsymbol{u}}. \tag{7}$$

Premultiplying equation (1) by the entropy variables $\boldsymbol{w}^T$ and integrating it over a control volume Ω with boundary $\partial\Omega$ and applying the divergence theorem yields

$$\int_\Omega \frac{\partial U}{\partial t}\,\mathrm{d}V + \int_{\partial\Omega} \left(\boldsymbol{\mathcal{F}}(\boldsymbol{u}) - \boldsymbol{w}^T \boldsymbol{K}\nabla\boldsymbol{w}\right)\cdot \boldsymbol{n}\,\mathrm{d}S = -\int_\Omega \boldsymbol{K}\nabla\boldsymbol{w} : \nabla\boldsymbol{w}\,\mathrm{d}V, \tag{8}$$

where $\boldsymbol{K}$ is the Jacobian of the diffusive flux with respect to the gradients of the entropy variables. By construction, $\boldsymbol{K}$ is a symmetric and positive semi-definite matrix [29]; hence the last term is always non-positive. Therefore, the net contribution of any process within the control volume is to reduce the mathematical entropy, with the only way to increase it being through a net flux across the boundary. By enforcing appropriate boundary conditions, the entropy inequality is given by

$$\frac{\mathrm{d}}{\mathrm{d}t}\int_\Omega U(\boldsymbol{u})\,\mathrm{d}V \leq 0. \tag{9}$$

This property ensures that the mathematical entropy of the system is non-increasing in time and therefore introduces a bound for the energy of the real solution [30, 31], as

constrained by the boundary conditions. The existence of U guarantees the uniqueness of the weak solution. The discrete equivalent of this equation is used to stabilize the discretization of the Euler and Navier-Stokes equations for transonic and supersonic flows, ensuring convergence to the correct weak solution. Its application to the discontinuous Galerkin method is explained in Section 3.3.

The transformation from conservative to entropy variables is given by

$$\boldsymbol{w}(\boldsymbol{u}) = \begin{pmatrix} w_1 \\ w_{1+i} \\ w_{d+2} \end{pmatrix} = \begin{pmatrix} \frac{\rho e(\gamma+1-s)-\rho E}{\rho e} \\ \frac{\rho v_i}{\rho e} \\ -\frac{\rho}{\rho e} \end{pmatrix}, \tag{10}$$

and from entropy to conservative variables by

$$\boldsymbol{u}(\boldsymbol{w}) = \begin{pmatrix} \rho \\ \rho v_i \\ \rho E \end{pmatrix} = \begin{pmatrix} -(\rho e) w_{d+2} \\ (\rho e) w_{1+i} \\ (\rho e)\left(1 - \frac{\sum_{j=1}^{d} w_{1+j}^2}{2 w_{d+2}}\right) \end{pmatrix}. \tag{11}$$

The internal energy density ρe and the physical entropy s can also be derived in terms of the entropy variables

$$\rho e = \left(\frac{\gamma - 1}{(-w_{d+2})^{\gamma}}\right)^{\frac{1}{\gamma-1}} \exp\left(\frac{-s}{\gamma - 1}\right), \quad s = \gamma - w_1 + \frac{\sum_{j=1}^{d} w_{1+j}^2}{2 w_{d+2}}. \tag{12}$$

3. Numerical methods

All the simulations presented in this work were performed using a high-order Cartesian solver based on the discontinuous Galerkin Spectral Element (DG) method. Different variants of the DG method are considered to assess their performance on the compressible Navier-Stokes equations. Unless otherwise specified, all variants are based on Gauss-Legendre quadrature and therefore the Gauss-Legendre shape functions. The following methods are evaluated in this study:

- the vanilla DG method (DG),
- the DG method with Laplacian artificial viscosity (DG-AV),
- the entropy-stable DG method based on the SBP operator and the entropy variables (ESDG-GL),
- the entropy-stable DG method based on the Gauss-Lobatto polynomial (ESDG-GLL),
- a novel approach proposed in this work, the local entropy-stable DG method (DG-ES) based on the troubled cells detection and activation of the entropy stability in the vicinity of under-resolved features (similar to the artificial viscosity principle).

The following section introduces the necessary definitions and provides a succinct overview of each method.

3.1. Some definitions

The discretization of equation (1) is based upon a tessellation ε, consisting of elements $\mathcal{K}$, of the domain Ω, such that $\Omega \sim \varepsilon = \cup\mathcal{K}$. The trial space $(\mathcal{V}^{\mathrm{p}})^{N_v}$ used for all discontinuous Galerkin methods in this work consists of p-degree polynomial approximations on a reference element $\widehat{\mathcal{K}}$, for each of the N_v variables in system (1). Since the same basis functions are used for all variables, we restrict our attention to the trial space $\mathcal{V}^{\mathrm{p}}$ in the following definitions. As only tensor product reference elements (quadrilaterals in 2D and hexahedra in 3D) are considered, the natural polynomial space on a d-dimensional element is the space of maximum degree p polynomials

$$Q^{\mathrm{p}}(\widehat{\mathcal{K}}) = \left\{ \widehat{x}_1^{i_1} \dots \widehat{x}_d^{i_d}, \quad \widehat{\boldsymbol{x}} \in \widehat{\mathcal{K}}, \quad 0 \leq i_k \leq \mathrm{p}, \quad k = 1, \dots, d \right\}.$$

Let $\widehat{f}$ denote a face belonging to the reference element $\widehat{\mathcal{K}}$. The trace space $\mathcal{V}^{\mathrm{p}}\left(\widehat{f}\right)$ is defined as the set of functions in $\mathcal{V}^{\mathrm{p}}\left(\widehat{\mathcal{K}}\right)$ restricted to $\widehat{f}$

$$\mathcal{V}^{\mathrm{p}}(\widehat{f}) = \left\{ q|_{\widehat{f}}, \quad q \in \mathcal{V}^{\mathrm{p}}(\widehat{\mathcal{K}}), \quad \widehat{f} \in \partial\widehat{\mathcal{K}} \right\}.$$

For the d-dimensional tensor product element considered here, the trace space $\mathcal{V}^{\mathrm{p}}\left(\partial\widehat{\mathcal{K}}\right)$ is composed of polynomials with a maximum degree p over a tensor product of dimension $(d-1)$.

A set of linearly independent functions, called *shape functions*, is chosen to form a basis for $\mathcal{V}^{\mathrm{p}}$. The shape functions provide a local support in the context of the discontinuous Galerkin method, allowing the solution to be discontinuous between the elements. Hence, for each element, $N_\phi = \dim\left(\mathcal{V}^{\mathrm{p}}\left(\widehat{\mathcal{K}}\right)\right)$ is the local number of unknowns per variable. By choosing the shape functions ϕ_i of $\mathcal{V}^{\mathrm{p}}\left(\widehat{\mathcal{K}}\right)$, the discrete approximation of any variable $\boldsymbol{q}$, $\boldsymbol{q}_h$, can be expressed as

$$\boldsymbol{q}_h(\boldsymbol{x}, t) = \sum_i^{N_\phi} \phi_i(\boldsymbol{x}) \boldsymbol{q}_i(t).$$

Note that at this stage, we do not specify the set of variables $\boldsymbol{q}_h$ which can either be the conservative $\boldsymbol{u}_h$ or entropy variables $\boldsymbol{w}_h$.

The basis functions used in this work are the Lagrange interpolants, and the interpolation points are defined either by the Gauss-Legendre (GL) or by the Gauss-Lobatto (GLL) quadrature points. The integrations are performed by using quadrature rules $\left(\widehat{\boldsymbol{\xi}}_v, w_v\right)$ and $\left(\widehat{\boldsymbol{\xi}}_f, w_f\right)$, where $\widehat{\boldsymbol{\xi}}_v$ and $\widehat{\boldsymbol{\xi}}_f$ are the volume and surface quadrature points, respectively, and w_v and w_f represent the volume and surface quadrature weights. The specifications of these quadrature rules may differ based on the DG variants and will be explicitly stated later.

Let us define the interpolation matrices $\boldsymbol{C}_v$ and $\boldsymbol{C}_f$, which map the basis coefficients from the interpolation to the quadrature points

$$(\boldsymbol{C}_v)_{qi} = \phi_i(\widehat{\boldsymbol{\xi}}_v), \quad (\boldsymbol{C}_f)_{qi} = \phi_i(\widehat{\boldsymbol{\xi}}_f). \tag{13}$$

The collocated solutions at the volume and surface quadrature points, $\left(\boldsymbol{q}_v, \boldsymbol{q}_f\right)$, are given respectively by

$$\boldsymbol{q}_v = (\boldsymbol{C}_v)_{qi}\boldsymbol{q}_i, \quad \boldsymbol{q}_f = (\boldsymbol{C}_f)_{qi}\boldsymbol{q}_i. \tag{14}$$

The mass matrix $\boldsymbol{M}$ can be assembled as

$$\boldsymbol{M} = \boldsymbol{C}_v^T \boldsymbol{W} \boldsymbol{C}_v \tag{15}$$

where $\boldsymbol{W}$ is the diagonal matrix of the volume quadrature weights. In the Spectral Element Method, the volume quadrature points coincide with the interpolation points. This simplifies the interpolation matrix $\boldsymbol{C}_v$ to the identity matrix, and consequently, the mass matrix reduces to $\boldsymbol{M} = \boldsymbol{W}$.

Let $\boldsymbol{D}_v^k$ and $\boldsymbol{D}_f^k$ denote the gradient interpolation matrices, which map the basis coefficients of a function from the interpolation points to the basis coefficients of its derivative in the kth direction at the volume and surface quadrature points

$$(\boldsymbol{D}_v^k)_{qi} = \frac{\partial \phi_i}{\partial \xi^k}\left(\widehat{\boldsymbol{\xi}}_v\right), \quad (\boldsymbol{D}_f^k)_{qi} = \frac{\partial \phi_i}{\partial \xi^k}\left(\widehat{\boldsymbol{\xi}}_f\right). \tag{16}$$

Let $\boldsymbol{n}$ be the scaled normal vector pointing outward of the element $\widehat{\mathcal{K}}$,

$$\boldsymbol{n} = \{n_k J_f, \quad k = 1, ..., d\},$$

where J_f denotes the determinant of the Jacobian associated with the mapping from a face of $\partial\widehat{\mathcal{K}}$ to its corresponding reference face. Finally, $\boldsymbol{B}^k$ is the boundary integration matrix defined as

$$\boldsymbol{B}^k = \boldsymbol{W}_f \mathrm{diag}(\boldsymbol{n}_k). \tag{17}$$

3.2. Vanilla DG method

This section introduces the reference vanilla discontinuous Galerkin method described in [32, 33]. Multiplying equation (1) with any test function $\varphi \in \mathcal{V}^{\mathrm{p}}$ defined on the element and using the conservative variables $\boldsymbol{u}$ yields

$$\sum_{\mathcal{K}} \int_{\mathcal{K}} \varphi \left(\frac{\partial \boldsymbol{u}_h}{\partial t}\right) \mathrm{d}V + \sum_{\mathcal{K}} \int_{\mathcal{K}} \varphi \left(\nabla \cdot \boldsymbol{f}(\boldsymbol{u}_h)\right) \mathrm{d}V = \sum_{\mathcal{K}} \int_{\mathcal{K}} \varphi \left(\nabla \cdot \boldsymbol{d}(\boldsymbol{u}_h, \nabla \boldsymbol{u}_h)\right) \mathrm{d}V. \tag{18}$$

3.2.1. Convective term

By using integration by parts and replacing the boundary integral by the sum over all faces, the convective term, i.e., the second term in equation (18), becomes

$$\sum_{\mathcal{K}} \int_{\mathcal{K}} \varphi \nabla \cdot \boldsymbol{f}(\boldsymbol{u}_h) \ \mathrm{d}V = -\sum_{\mathcal{K}} \int_{\mathcal{K}} \nabla \varphi \cdot \boldsymbol{f}(\boldsymbol{u}_h) \ \mathrm{d}V + \sum_{f} \int_{f} [\varphi] \boldsymbol{f}^*(\boldsymbol{u}_h^+, \boldsymbol{u}_h^-; \boldsymbol{n}) \mathrm{d}S. \tag{19}$$

The jump operator for any state vector $\boldsymbol{a}$ is defined as $[\boldsymbol{a}] = \boldsymbol{a}^+ - \boldsymbol{a}^-$, where $\boldsymbol{a}^+$ and $\boldsymbol{a}^-$ are values on the element $\mathcal{K}$ from the interior and exterior of the face f, respectively. The numerical flux $\boldsymbol{f}^*$ used in this work is the local Lax-Friedrichs flux, defined as

$$\boldsymbol{f}^*(\boldsymbol{u}^+, \boldsymbol{u}^-; \boldsymbol{n}) = \frac{\boldsymbol{f}^{\boldsymbol{n}}(\boldsymbol{u}^+) + \boldsymbol{f}^{\boldsymbol{n}}(\boldsymbol{u}^-)}{2} + \max|\boldsymbol{\lambda}| \frac{\boldsymbol{u}^+ - \boldsymbol{u}^-}{2}, \tag{20}$$

where $\boldsymbol{\lambda}$ represents the characteristic wave speeds of the convective part of the Navier-Stokes equations (1). While the local Lax-Friedrichs flux is relatively dissipative, it significantly enhances the stability of the vanilla DG method and leads to accurate results, as shown in Section 4.

3.2.2. Diffusive term

The diffusive terms are discretized by using the *incomplete interior penalty method* (IIPM) developed in [1, 34] [1]

$$\begin{aligned}\sum_{\mathcal{K}} \int_{\mathcal{K}} \varphi \nabla \cdot \boldsymbol{d}(\boldsymbol{u}_h, \nabla \boldsymbol{u}_h)\, dV = &\sum_{\mathcal{K}} \int_{\mathcal{K}} \nabla\varphi\ \boldsymbol{d}(\boldsymbol{u}_h, \nabla \boldsymbol{u}_h)\, dV \\ &- \sum_{f} \int_{f} [\varphi]\{\boldsymbol{d}(\boldsymbol{u}_h, \nabla \boldsymbol{u}_h)\}\, dS \\ &+ \sum_{f} \int_{f} \sigma_f [\varphi][\boldsymbol{u}_h]\, dS, \end{aligned} \tag{21}$$

where σ_f is the penalty parameter. The average operator for any state vector $\boldsymbol{a}$ is defined as $\{\mathbf{a}\} = (\boldsymbol{u}^+ + \boldsymbol{u}^-)/2$. To ensure the coercivity of the bilinear form, the penalty parameter is chosen, for tensor product elements, as [1]

$$\sigma_f > \max_{\mathcal{K} \ni f} \left(n_f \rho(\boldsymbol{D}) (\mathrm{p}+1)^2 \frac{A(f)}{8V(\mathcal{K})} \right), \tag{22}$$

where p is the interpolation order, $A(f)$ is the area of the face, $V(\mathcal{K})$ is the volume of the element $\mathcal{K}$, n_f is the number of faces in the element $\mathcal{K}$ and the diffusive spectral radius is defined as $\rho(\boldsymbol{D}) = 2\mu + \kappa/c_v$.

3.2.3. Final formulation

Finally, by performing the integrations with the quadrature rules and using the matrix notation defined in Section 3.1, the vanilla discontinuous Galerkin method is given by

$$\begin{aligned}\boldsymbol{M} \frac{\partial \boldsymbol{u}_h}{\partial t} &- \sum_{k=1}^{d} \boldsymbol{W} (\boldsymbol{D}_v^k)^T \left[\boldsymbol{f}(\boldsymbol{u}_v) + \boldsymbol{d}(\boldsymbol{u}_v, \nabla \boldsymbol{u}_v) \right] \\ &+ \sum_{k=1}^{d} \boldsymbol{C}_f^T \boldsymbol{B}^k \left[\boldsymbol{f}_k^*(\boldsymbol{u}_f^+, \boldsymbol{u}_f^-; \boldsymbol{n}) + \{\boldsymbol{d}_k(\boldsymbol{u}_f, \nabla \boldsymbol{u}_f)\} - \sigma_f [\boldsymbol{u}_f] \right] = 0. \end{aligned} \tag{23}$$

For this method, the integration is performed using Gauss-Legendre quadrature, which yields exact integration for polynomials of degree up to $2N + 1$.

3.3. Entropy stable DG method based on Gauss-Legendre polynomial (ESDG-GL)

The introduction of high-order entropy stable discretization is motivated by the lack of robustness of the vanilla discontinuous Galerkin method in the presence of discontinuities such as shocks or under-resolved turbulence. The aim of this method is to satisfy a semi-discrete entropy inequality, thereby providing better control over the production and destruction of energy in the simulation. All entropy stable schemes are based on two main components:

[1] No improvement has been noticed by using the symmetric version of the IPM for all the methods presented in this work.

- The *entropy variables* are used to interpolate the solution $\boldsymbol{w}_h \in \mathcal{V}^{\mathrm{p}} : \boldsymbol{w}_h = \sum_i^{N_\phi} \phi_i(\boldsymbol{x}) \mathbf{w}_i(t)$. Since the variational formulation tests for any function in $\mathcal{V}^{\mathrm{p}}$, it can be weighted with the solution itself, i.e. the entropy variables, resulting in a discrete equivalent of the entropy conservation equations. This in turn allows controlling the evolution of the entropy of the solution [29, 28, 35].

- The non-linear convective terms are discretized using the *flux differencing* using *summation-by-parts* (SBP) differentiation operators which satisfy a discrete analogue of integration by parts [36, 17, 37], providing a rigorous discrete entropy conservation equation.

Integration by parts of equation (19) is avoided in entropy-stable schemes, with a preference for discretizing a differentiation matrix for the term $\nabla \cdot \boldsymbol{f}$ by performing a flux differencing operation $\boldsymbol{Q}_N^k \circ \boldsymbol{F}_S$, where $\circ$ denotes the Hadamard product. $\boldsymbol{Q}_N^k$ is an SBP operator and $\boldsymbol{F}_S$ is a two-argument matrix flux function based on a two-point entropy stable numerical flux $\boldsymbol{f}_S$ as defined by Tadmor [30]. In this work, the entropy conservative Chandrashekar flux is employed [38].

The skew-symmetric hybridized SBP operator $\boldsymbol{Q}_N^k$ from Chan [23] is used for this method. To prevent all-to-all element coupling and satisfy the chain rule in the case of Gauss-Legendre quadrature [39], this operator introduces a link between volume and surface quadrature

$$\boldsymbol{Q}_N^k = \begin{pmatrix} \boldsymbol{Q}^k - (\boldsymbol{Q}^k)^T & \boldsymbol{E}^T \boldsymbol{B}^k \\ -\boldsymbol{B}^k \boldsymbol{E} & 0 \end{pmatrix}, \tag{24}$$

where $\boldsymbol{Q}_k$ is the generalized SBP operator, $\boldsymbol{E}$ is an extrapolation matrix that maps basis coefficients from volume to surface quadrature points using $\boldsymbol{P}$, a quadrature-based L^2 projection matrix:

$$\boldsymbol{Q}^k = \boldsymbol{W} \boldsymbol{D}_v^k \boldsymbol{P}, \quad \boldsymbol{E} = \boldsymbol{C}_f \boldsymbol{P}, \quad \boldsymbol{P} = \boldsymbol{M}^{-1} \boldsymbol{C}_v^T \boldsymbol{W}. \tag{25}$$

The matrix formulation of equation (1) for the ESDG-GL is given by

$$\begin{aligned} \boldsymbol{M} \frac{\partial \boldsymbol{u}_h}{\partial t} + \sum_{k=1}^{d} \begin{bmatrix} \boldsymbol{C}_v \\ \boldsymbol{C}_f \end{bmatrix}^T \left(\boldsymbol{Q}_N^k \circ \boldsymbol{F}_S^k \right) \mathbf{1} - \sum_{k=1}^{d} \boldsymbol{W} (\boldsymbol{D}_v^k)^T \boldsymbol{d}(\boldsymbol{w}_v, \nabla \boldsymbol{w}_v) \\ + \sum_{k=1}^{d} \boldsymbol{C}_f^T \boldsymbol{B}^k \left[\boldsymbol{f}_{S,k}^*(\boldsymbol{w}_f^+, \boldsymbol{w}_f^-; \boldsymbol{n}) + \{\boldsymbol{d}_k(\boldsymbol{w}_f, \nabla \boldsymbol{w}_f)\} - \sigma_f [\boldsymbol{w}_f] \right] = 0, \\ (\boldsymbol{F}_S^k)_{ij} = \boldsymbol{f}_S^k(\boldsymbol{w}_i, \boldsymbol{w}_j), \quad 1 \leq i, j \leq N_q + N_q^f, \end{aligned} \tag{26}$$

where N_q and N_q^f represent the number of volume and surface quadrature points, respectively, and $\mathbf{1}$ is a vector of ones. At interfaces, a Lax-Friedrichs penalization is added to the entropy stable numerical flux to ensure stability,

$$\boldsymbol{f}_{S,k}^*(\boldsymbol{w}^+, \boldsymbol{w}^-) = \boldsymbol{f}_S^k \left(\{\boldsymbol{w}\}_{\log} \right) + \frac{\max |\boldsymbol{\lambda}|}{2} \left(\boldsymbol{w}^+ - \boldsymbol{w}^- \right). \tag{27}$$

Finally, to ensure that equation (26) enforces the entropy inequality (9), it is necessary to employ the projected entropy variables $\boldsymbol{w}_h$ at the quadrature points, as demonstrated by Chan *et al.* [23]. This set of variables is obtained as follows:

- computation of the entropy variables from the conservative variables at the volume quadrature points $\boldsymbol{w}_v = \boldsymbol{w}(\boldsymbol{u_v})$,
- projection of the entropy variables to the functional basis and interpolation to the volume and surface quadrature points $\tilde{\boldsymbol{w}} = \begin{bmatrix} \boldsymbol{C}_v \\ \boldsymbol{C}_f \end{bmatrix} \boldsymbol{P}\boldsymbol{w}_v$,
- conversion of the entropy variables at quadrature points to conservative variables $\boldsymbol{w}_h = \boldsymbol{u}(\tilde{\boldsymbol{w}})$. This step is not strictly necessary; however, it enables the use of the same flux functions for both the entropy-stable schemes and the vanilla DG method.

The discretized evolution equations provide the time change of the conservative variables, rather than the entropy variables, and is expressed with the same basis functions. Due to the non-linearity of the relation between the conservative and entropy variables, the conversion to the entropy variables through the so-called *entropy projection* is not fully accurate and introduces a source of error, as observed in Section 4.

3.4. Entropy stable DG method based on Gauss-Lobatto polynomial (ESDG-GLL)

An interesting variant to the entropy stable method based on the Gauss-Legendre quadrature is the entropy stable scheme based on the Gauss-Lobatto quadrature, providing the advantage of having interpolation points directly located on the boundaries. Consequently, numerous matrices simplify to identity matrices, such as the face interpolation matrix $\boldsymbol{C}_f$, and the extraction matrix $\boldsymbol{E}$. As the quadrature incorporates points on the boundary, connecting volume and surface quadrature rules is no longer necessary, allowing the use of the generalized SBP operator $\boldsymbol{Q}^k$ for flux differencing operations. Therefore, the matrix formulation of equation (1) for the ESDG-GLL is given by

$$\begin{aligned} &\boldsymbol{M}\frac{\partial \boldsymbol{u}_h}{\partial t} + \sum_{k=1}^{d} \left((\boldsymbol{Q}^k - (\boldsymbol{Q}^k)^T) \circ \boldsymbol{F}_S^k \right) \boldsymbol{1} - \sum_{k=1}^{d} \boldsymbol{W} (\boldsymbol{D}_v^k)^T \left[\boldsymbol{d}(\boldsymbol{u}_v, \nabla \boldsymbol{u}_v) \right] \\ &+ \sum_{k=1}^{d} \boldsymbol{B}^k \left[\boldsymbol{f}_{S,_k}^*(\boldsymbol{u}_f^+, \boldsymbol{u}_f^-; \boldsymbol{n}) + \{ \boldsymbol{d}_k(\boldsymbol{u}_f, \nabla \boldsymbol{u}_f) \} - \sigma_f [\boldsymbol{u}_f] \right] = 0, \\ &(\boldsymbol{F}_S^k)_{ij} = \boldsymbol{f}_S^k(\boldsymbol{u}_i, \boldsymbol{u}_j), \quad 1 \leq i, j \leq N_q. \end{aligned} \tag{28}$$

The entropy projected variables are equal to the conservative variables for equation (28) due to the one-to-one mapping defined in equations (10-11). The main drawback of the ESDG-GLL is the lower integration accuracy of the Gauss-Lobatto quadrature, which is only exact up to a $(2N-1)$ polynomial. This issue leads to effects such as aliasing in the simulation.

3.5. Discontinuous Galerkin method with artificial viscosity (DG-AV)

The artificial viscosity method used in this work is based on the Laplacian method from Persson and Peraire [15]. The detection of the troubled cells is performed using the Hennemann sensor [40] based on the regularity criterion of the solution from Persson and Peraire [15]. The amount of under-resolution is estimated by comparing the energy in

the highest polynomial over the energy of the solution. This method defines a blending function $\alpha \in [0, 1]$ as

$$\alpha = \frac{1}{1 + \exp\left(\frac{-s}{\mathcal{T}}\left(\mathcal{E} - \mathcal{T}\right)\right)}, \tag{29}$$

where the sharpness factor $s = 9.21024$, the threshold $\mathcal{T} = 0.5 \cdot 10^{-1.8(\mathrm{p}+1)^{\frac{1}{4}}}$. To prevent unnecessary activation of the sensor, a minimum cutoff value $\alpha_{\min} = 0.001$ is introduced, such that the modified sensor value is defined as $\alpha = \max(\alpha - \alpha_{\min}, 0)$. The energy indicator $\mathcal{E}$ is given on an element by

$$\mathcal{E} = \frac{(q - \hat{q}, q - \hat{q})_{\mathcal{K}}}{(q, q)_{\mathcal{K}}}, \tag{30}$$

where $(.,.)_{\mathcal{K}}$ is the inner product in L_2, q is the full expansion up to order p of the indicator variable and $\hat{q}$ is the truncated expansion up to order $\mathrm{p} - 1$ of the same variable. In this work, the indicator variable is the density. A comparison between different detectors is performed in Section 4.1.5. The diffusive term in equation (1) is modified by adding the artificial viscosity term $\nabla \cdot (\mu_{\mathrm{av}} \nabla u)$, where μ_{av} is the artificial viscosity defined as

$$\mu_{\mathrm{av}} = \alpha \mu_{\mathrm{av},0}, \quad \mu_{\mathrm{av},0} = c \frac{h}{p} \lambda_{\max}. \tag{31}$$

$\mu_{\mathrm{av},0}$ represents the maximum artificial viscosity that can be applied within an element, h denotes the element size and $\lambda_{\max}$ is the maximum wave speed. The scaling factor c is defined based on the recommendations of Vandenhoeck *et al.* [41], eliminating the need for parameter tuning, as $c = 0.27 \frac{M_\infty - 1}{M_\infty}$ where M_∞ is the freestream Mach number. To ensure positivity, M_∞ is bounded below by 1.2.

3.6. Discontinuous Galerkin method with entropy stability (DG-ES)

The aim of the novel DG-ES method is to activate entropy stability discretization (entropy variables and SBP operator) only in the vicinity of under-resolved features, such as shocks or regions with high gradients. This approach leverages the high accuracy of the discontinuous Galerkin method while ensuring the robustness provided by entropy-stable schemes. As demonstrated in Section 4, entropy variables can negatively impact the solution compared to the vanilla DG method when applied globally. Therefore, by selectively applying entropy stability only where necessary, the DG-ES method achieves an optimal balance between accuracy and stability, making it particularly suited for problems with localized under-resolved regions. Additionally, the computational cost remains controlled, as entropy stability is applied judiciously, avoiding excessive stabilization. Troubled cells are identified using the Hennemann sensor, as detailed in equation (29) for the DG-AV method. The discretization of normal cells follows equation (23), while troubled cells are discretized using equation (26).

4. Numerical results

This section presents the numerical results obtained from various under-resolved test cases designed to evaluate the performance of the methods considered. The focus is on assessing the accuracy, robustness, and computational efficiency of the stabilization

techniques in different flow scenarios. Accuracy is assessed by comparing the numerical results to reference solutions obtained from high-resolution simulations, using metrics such as the kinetic energy budget, density profiles, and Reynolds stresses. Robustness is evaluated in both spatial and temporal dimensions: spatial robustness is evaluated through mesh refinement studies, while temporal robustness is measured by identifying the maximum stable CFL number that can be used without simulation failure, computed as [42]

$$\mathrm{CFL} = \Delta t \frac{2\mathrm{p}+1}{h}\left(\max|\boldsymbol{\lambda}| + d\cdot\rho(\boldsymbol{D})\frac{2\mathrm{p}+1}{h}\right). \tag{32}$$

The CFL number is defined based on the initial conditions of the test cases, and the time step is considered constant throughout the simulation[2]. Computational efficiency is assessed by normalizing the total simulation time with respect to the least expensive method. The four test cases correspond to compressible homogeneous isotropic turbulence, the Taylor-Green vortex at a Mach number $M_0 = 1.25$, strong-vortex/shock interaction and shock-turbulence interaction.

4.1. Compressible Homogeneous Isotropic Turbulence

The objective of this test case is to evaluate the accuracy, robustness and computational cost of the shock capturing methods in the presence of under-resolved compressible turbulence. In this paper, the decay of compressible homogeneous isotropic turbulence with eddy shocklets is considered [14, 44, 45, 19, 16, 46] to ensure the activation of the numerical dissipation mechanisms.

4.1.1. Case description and computational setup

The computational domain is a cube $\Omega = [-L\pi, L\pi]^3$ with periodic boundary conditions in all directions. The characteristic length scale L is set to $L = 1$. The procedure to generate the initial conditions is explained in Johnsen *et al.* [47]. The initial density, pressure, and temperature fields are uniform, and the velocity field is solenoidal. The initial kinetic energy spectrum is given as $E(\tilde{k}) \sim \tilde{k}^4 \exp[-2(\tilde{k}/\tilde{k}_M)^2]$, where $\tilde{k}_M = 4/L$ is the most energetic wavenumber. The initial turbulent Mach number is $M_{t,0} = \sqrt{\langle v_{i,0} v_{i,0}\rangle}/\langle c_0\rangle = 0.6$ and the initial Taylor-scale Reynolds number is $Re_{\lambda,0} = \langle\rho_0\rangle v_{\mathrm{rms},0}\lambda_0/\langle\mu_0\rangle = 100$, where the subscript zero is for the initial values, $\langle\cdot\rangle$ is the spatial average and c_0 is the initial speed of sound. The root-mean-square velocity and the Taylor microscale are defined by $v_{\mathrm{rms}} = \sqrt{\langle v_i v_i\rangle/3}$, and $\lambda = \sqrt{\langle v_1^2\rangle/\langle(\partial_1 v_1)^2\rangle}$, respectively. The chosen energy spectrum results in $\lambda_0 = 2/\tilde{k}_M$. To conclude the non-dimensional description of the problem, the shear viscosity is assumed to follow a power-law given by $\mu(T) = \mu_0\left(\frac{T}{T_0}\right)^{3/4}$ and the initial eddy turn-over time is given by $\tau_0 = \lambda_0/v_{\mathrm{rms},0}$. The Prandtl number is set to $Pr = 0.71$ and the specific heat ratio is $\gamma = 1.4$.

The RK(4,4) time integration scheme is used with a fixed time step of $\Delta t = 5\cdot10^{-3}\tau_0$, leading to a CFL number CFL = 0.16. The simulations are performed from $t_0 = 0$ to

[2]The primary goal is not to determine an absolute CFL value, but to enable a fair comparison of the different methods under a consistent definition. For a detailed and rigorous definition, the reader is referred to the work of Chan *et al.* [43].

$t_f = 4\tau_0$. The computational domain is discretized into a uniform 11^3 Cartesian grid with an interpolation order p = 5, leading to 66^3 degrees of freedom (DOF). Although this setup leads to severe spatial under-resolution, Hillewaert *et al.* [14] have shown that the vanilla DG method does not require additional stabilization mechanisms. Hence, the impact of the entropy stable scheme, the SBP operator, and artificial viscosity on the accuracy of the method can be assessed. The results are compared to the direct numerical simulation from Hillewaert *et al.* [14] with a resolution of 1920^3 DOF.

4.1.2. Numerical results

Figure 1 illustrates the time evolution of the volume-averaged mean-square velocity, vorticity, temperature fluctuations, and dilatation fluctuations ($\theta = \nabla \cdot \mathbf{u}$). Despite the level of under-resolution in the simulations, there is an overall good agreement with the DNS solution. The full entropy stable methods, ESDG-GL and ESDG-GLL, show good agreement with the vanilla DG method for the mean-square velocity, temperature, and dilatation fluctuations. However, these methods tend to dampen the vortical structures and underestimate the peak of mean-square vorticity. While this behavior is expected for the ESDG-GLL due to its lower quadrature order, it is surprising for the ESDG-GL method, which had been anticipated to match the vanilla DG method. Since the conservative variables and the test functions are polynomial, but the entropy variables are not, projecting the entropy variables onto the polynomial space introduces numerical error. To mitigate this issue, over-integration can be performed; however, this significantly degrades computational performance. Our alternative, the DG-ES method, improves the accuracy of the ESDG-GL method by applying the SBP operator and the entropy projection only in the vicinity of under-resolved features. Interestingly, the DG-AV method performs better than the full entropy-stable schemes and shows similar results to the DG-ES method. For this case, both methods detect a maximum of $\sim 10\%$ of the elements as troubled cells.

Figure 2 shows the temporal evolution of the measured rate of change of density-weighted kinetic energy, computed via finite differences between consecutive time steps, theoretical dissipation $\epsilon_t = \epsilon_2 + \epsilon_3 + \epsilon_4 + \epsilon_5$ as defined in equation (4), pressure dilatation, and the budget error for the compressible homogeneous isotropic turbulence problem. The budget error is defined as the difference between the measured rate of change of density-weighted kinetic energy and the theoretical dissipation. Among all methods, the vanilla DG approach exhibits the smallest budget error, in agreement with the results in Figure 1. In contrast, both ESDG methods overestimate the measured rate of change of density-weighted kinetic energy during the initial acoustic transient and throughout the early part of the simulation, from $t/\tau_0 = 0.8$ to 2. In the later stages, from $t/\tau_0 = 2.5$ to the end, they underestimate the theoretical dissipation due to the damping of vortical structures. As a result, the ESDG schemes show the largest budget errors, particularly the ESDG-GL, highlighting the influence of entropy projection on numerical accuracy. The DG-ES and DG-AV methods yield results similar to the vanilla DG, suggesting that applying entropy-stabilizing schemes or artificial viscosity selectively, only near under-resolved features, can preserve the favorable behavior of the baseline method.

4.1.3. Numerical stability

Table 1 provides the impact of different features on the numerical stability of the simulations. The simulations were performed with approximately the same number of

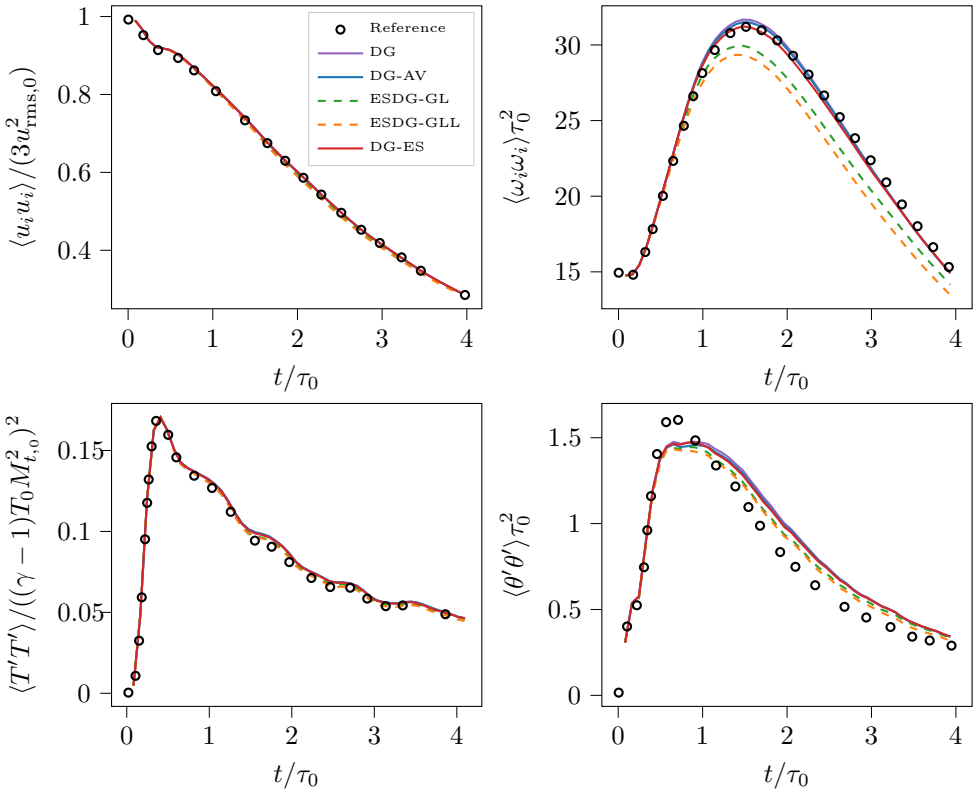

Figure 1: Temporal evolution of the volume-averaged mean-square velocity, vorticity, temperature variance and dilatation variance for the compressible homogeneous isotropic turbulence problem at $Re_{\lambda,0} = 100$ and $M_{t,0} = 0.6$ with $\mathrm{p} = 5$ and 11^3 elements.

degrees of freedom ($\sim 16^3 - 32^3 - 64^3$) at different interpolation orders $\mathrm{p} = 3, 4, 5$. As expected, the vanilla DG discretization is the most unstable and results in the divergence of the simulation at the lowest grid resolution. The use of either artificial viscosity or entropy stability is mandatory to stabilize the simulation at low resolution. The entropy stable schemes are always stable, even when applied locally. Hence, it appears sufficient to satisfy the second law of thermodynamics only in the troubled cells to improve the stability of the method.

Table 2 presents the maximum stable time step at different grid resolution. The results highlight that methods incorporating an entropy projection exhibit more restrictive time step constraints compared to the other approaches.

4.1.4. Computational cost

This section investigates the computational cost of the proposed methods. To this end, a dual-socket compute node with two AMD EPYC 7763 64-core processors and 256 GiB RAM was used. The computational cost of the different methods is normalized by the cost of the vanilla DG method. The results are summarized in Table 3. The ESDG-GL approach using the SBP operator with the Gauss-Legendre quadrature is the

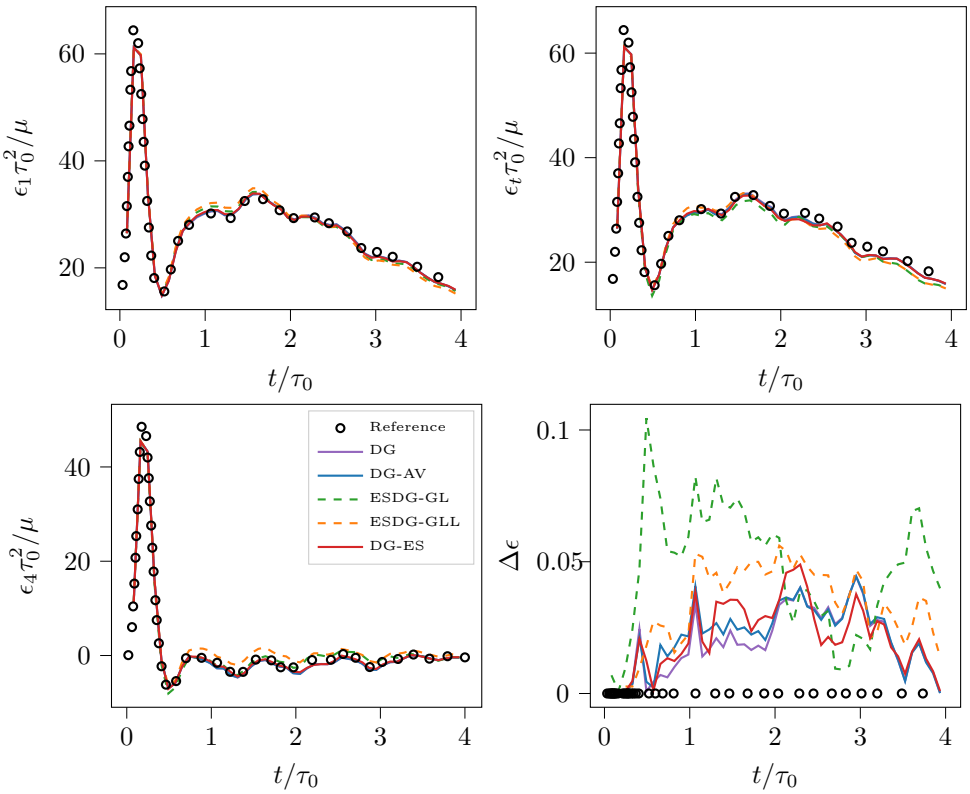

Figure 2: Temporal evolution of the measured rate of change of density-weighted kinetic energy (top left), the theoretical dissipation (top right), the pressure dilatation (bottom left) and the budget error (bottom right) for the compressible homogeneous isotropic turbulence problem at $Re_{\lambda,0} = 100$ and $M_{t,0} = 0.6$ with $\mathrm{p} = 5$ and 11^3 elements.

	$\mathrm{p}=3$			$\mathrm{p}=4$			$\mathrm{p}=5$		
	4^3	8^3	16^3	3^3	6^3	13^3	3^3	5^3	11^3
DG	✗	✗	✓	✗	✗	✓	✗	✗	✓
DG-AV	✓	✓	✓	✓	✓	✓	✓	✓	✓
ESDG-GLL	✓	✓	✓	✓	✓	✓	✓	✓	✓
ESDG-GL	✓	✓	✓	✓	✓	✓	✓	✓	✓
DG-ES	✓	✓	✓	✓	✓	✓	✓	✓	✓

Table 1: Numerical stability for the compressible homogeneous isotropic turbulence at $Re_{\lambda,0} = 100$ and $M_{t,0} = 0.6$ for different grid resolutions at the fixed time step $\Delta t = 5 \cdot 10^{-3}\tau_0$ (p is the interpolation order and the values below denote the number of elements). ✓: stable; ✗: unstable.

most computationally expensive. The SBP operator requires $O(\mathrm{p}^4)$ two-point inviscid flux evaluations (coupling both the surface and volume quadrature points) compared to the $O(\mathrm{p}^3)$ single-point flux evaluations (only at the volume quadrature points) for the

	DG	DG-AV	DG-ES	ESDG-GL	ESDG-GLL
p = 5, 3^3	/	0.31	0.19	0.19	0.28
p = 5, 5^3	/	0.28	0.22	0.22	0.29
p = 5, 11^3	0.23	0.23	0.18	0.18	0.27

Table 2: Maximum stable CFL for the compressible homogeneous isotropic turbulence at $Re_{\lambda,0} = 100$ and $M_{t,0} = 0.6$ for different grid resolutions (p is the interpolation order and the right value denotes the number of elements).

vanilla DG method. The entropy projection in the ESDG-GL method also increases the computational cost. The ESDG-GLL method, which uses the SBP operator and Gauss-Lobatto quadrature, does not require the coupling between the surface and volume quadrature points, nor the entropy projection, resulting in a lower cost compared to the ESDG-GL method. The DG-ES method significantly reduces the computational cost of the ESDG-GL method, although the cost can vary depending on the number of troubled cells. The DG-AV method has a computational cost close to that of the vanilla DG method, as artificial viscosity does not modify the discretization of the method.

	DG	DG-AV	DG-ES	ESDG-GL	ESDG-GLL
p = 3, 16^3	1	1.07	1.25	2.27	1.24
p = 4, 13^3	1	1.07	1.25	2.25	1.30
p = 5, 11^3	1	1.08	1.27	2.19	1.53

Table 3: Computational cost of the different methods normalized by the cost of the vanilla DG method for the compressible homogeneous isotropic turbulence at $Re_{\lambda,0} = 100$ and $M_{t,0} = 0.6$ at different grid resolutions (p is the interpolation order and the right value denotes the number of elements). CPU: 2x AMD EPYC 7763 64-core @2.45 GHz.

4.1.5. Impact of the detector

Figure 3 illustrates the impact of different detectors on the mean-square vorticity and dilatation fluctuations for the DG-AV and DG-ES methods. Three detectors are employed for the Laplacian artificial viscosity:

- The regularity criterion based on Persson and Peraire calibration (PP) [15].
- The regularity criterion based on Hennemann calibration (H) [40] and explained in Section 3.5.
- The shock sensor based on local flow features such as dilatation and vorticity [16].

The sensors based on the regularity criterion yield an elementwise artificial viscosity (constant within each element), while the shock sensor yields a subcellwise artificial viscosity. Only the two regularity-based detectors are employed for the DG-ES scheme. The detectors have not been fine-tuned for this problem; standard values of the parameters are used [15, 16, 41].

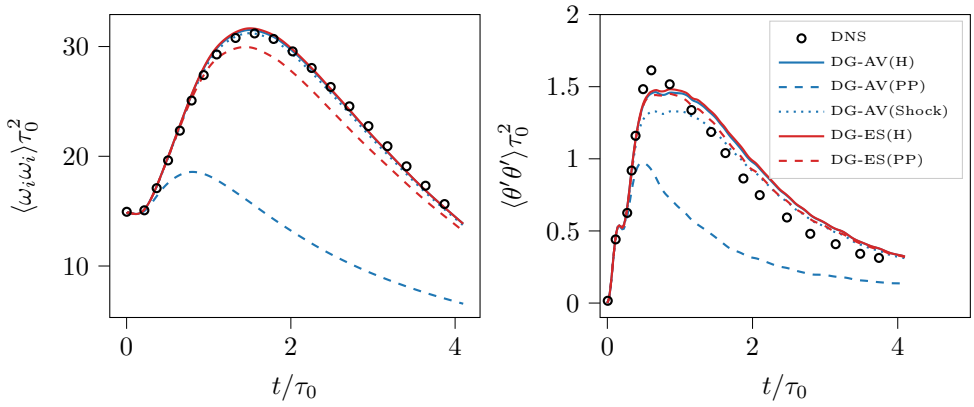

Figure 3: Temporal evolution of the mean-square vorticity (left) and dilatation fluctuations (right) for the DG-AV and DG-ES methods with various detectors for the compressible homogeneous isotropic turbulence problem at $Re_{\lambda,0} = 100$ and $M_{t,0} = 0.6$ with p = 5 and 11^3 elements.

The results show the significant sensitivity of the DG-AV method to the choice of detector, consistent with previous findings [16, 48]. In contrast, our method, DG-ES, demonstrates greater insensitivity to the choice of detector and, in the worst case, provides results comparable to those of the full ESDG-GL method, highlighting its robustness and reliability.

While the shock sensor yields similar mean square vorticity levels to the Hennemann-based detector, it introduces significantly higher dissipation in dilatation fluctuations. This is likely due to its reliance on local flow features, such as shocklets, that persist throughout the simulation. As a result, the shock sensor is triggered in a larger number of cells, leading to the application of excessive artificial viscosity, as shown in Figure 4. Among the regularity-based detectors, the Hennemann calibration clearly outperforms the original Persson and Peraire formulation, which tends to flag nearly all cells as troubled and thus introduces excessive dissipation.

Table 4 shows that regularity-based sensors offer greater numerical stability compared to the shock sensor. Overall, these findings confirm that regularity-based detectors, properly calibrated, can improve the performance of the DG-AV method while maintaining robustness.

	p = 3			p = 4			p = 5		
	4^3	8^3	16^3	3^3	6^3	13^3	3^3	5^3	11^3
Persson and Peraire	✓	✓	✓	✓	✓	✓	✓	✓	✓
Hennemann	✓	✓	✓	✓	✓	✓	✓	✓	✓
Shock sensor	✗	✓	✓	✗	✗	✓	✗	✗	✓

Table 4: Numerical stability of the various DG-AV simulations for the compressible homogeneous isotropic turbulence problem at $Re_{\lambda,0} = 100$ and $M_{t,0} = 0.6$ at the fixed time step $\Delta t = 5 \cdot 10^{-3} \tau_0$. ✓: stable; ✗: unstable.

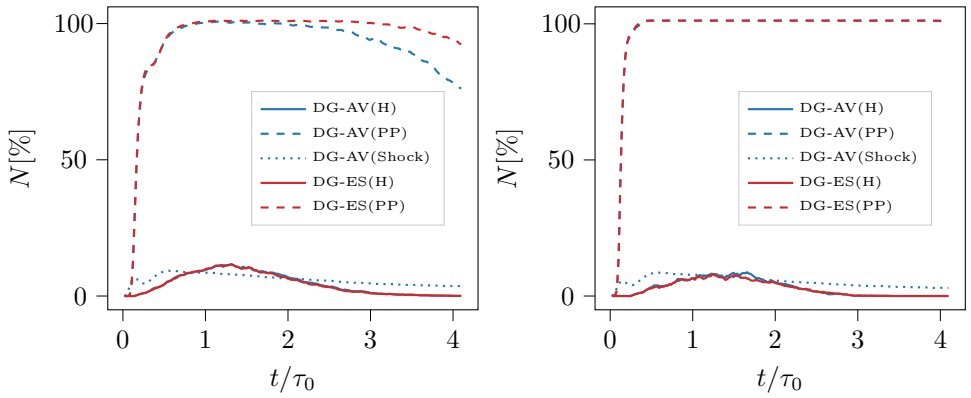

Figure 4: Temporal evolution of the percentage of troubled cells for the compressible homogeneous isotropic turbulence problem at $Re_{\lambda,0} = 100$ and $M_{t,0} = 0.6$. Results are shown for two configurations: 16^3 elements with polynomial order p = 3 (left), and 11^3 elements with p = 5 (right).

Finally, the behavior of the DG-ES and DG-AV methods is analyzed with respect to the choice of interpolation and quadrature points. Specifically, the DGSEM basis is compared to a standard non-collocated basis, in which the solution variables are stored at the interpolation points corresponding to Gauss–Lobatto nodes and subsequently interpolated to the quadrature points corresponding to Gauss–Legendre nodes. The results shown in Figure 5 indicate that the DG-ES method exhibits minimal sensitivity to the choice of interpolation and quadrature points. In contrast, the DG-AV method, somewhat unexpectedly, demonstrates a pronounced sensitivity to this distinction.

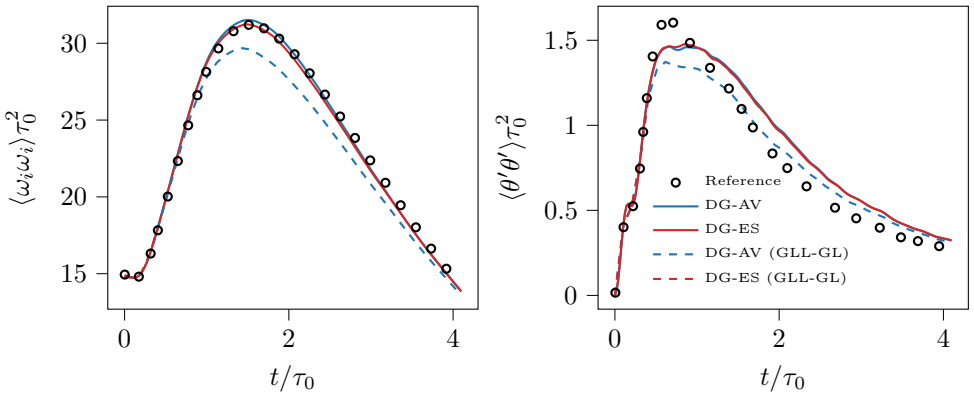

Figure 5: Temporal evolution of the percentage of troubled cells for the compressible homogeneous isotropic turbulence problem at $Re_{\lambda,0} = 100$ and $M_{t,0} = 0.6$ using 11^3 elements with p = 5. Two discretizations are compared: the DGSEM basis and a standard non collocated basis with Gauss-Lobatto interpolation points and Gauss-Legendre quadrature points.

4.2. Taylor-Green Vortex

The Taylor-Green vortex [49] is a well-known benchmark problem for the transition to turbulence, as depicted in Figure 6. The incompressible case has been extensively studied in the literature [2, 50, 51]. Recently, several works have focused on compressible variants at both low Reynolds number ($Re = 400$) [52, 53], and higher Reynolds number ($Re = 1600$) [54, 27, 55]. In this article, we consider the compressible Taylor-Green vortex at an initial Mach number $M_0 = 1.25$ and Reynolds number $Re = 1600$ to assess the performance of the methods across a wide range of scales.

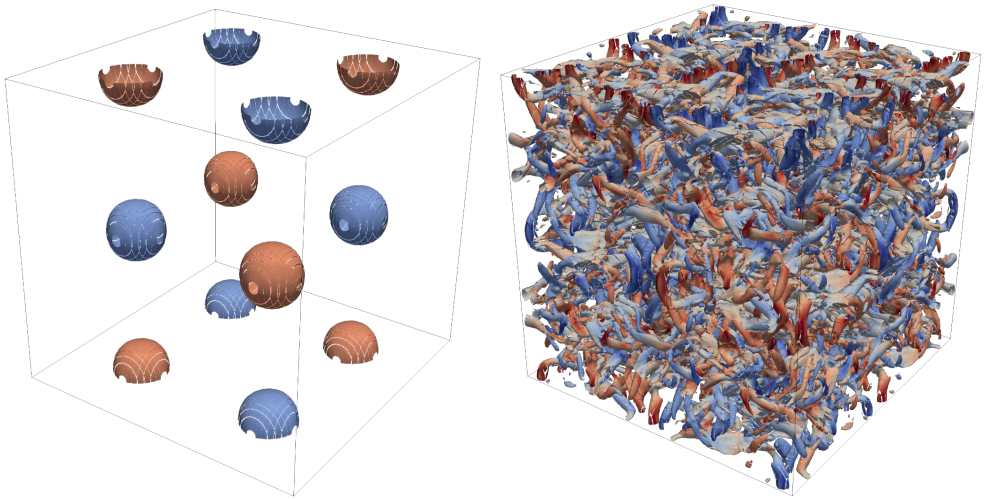

Figure 6: Q-criterion iso-surfaces colored by the z-component of the vorticity for the 3D Taylor-Green vortex at $Re = 1600$ and $M_0 = 1.25$ extracted from a 256^3 DOF simulation using the vanilla DG method. On the left, $t/t_c = 0$, and on the right, $t/t_c = 20$.

4.2.1. Case description and computational setup

The computational domain is a cube $\Omega = [-L\pi, L\pi]^3$ with triply-periodic boundary conditions. The analytical initial conditions of the Taylor-Green vortex are given by:

$$u(x, y, z, t = 0) = V_0 \sin\left(\frac{x}{L}\right) \cos\left(\frac{y}{L}\right) \cos\left(\frac{z}{L}\right), \tag{33}$$

$$v(x, y, z, t = 0) = V_0 \cos\left(\frac{x}{L}\right) \sin\left(\frac{y}{L}\right) \cos\left(\frac{z}{L}\right), \tag{34}$$

$$w(x, y, z, t = 0) = 0, \tag{35}$$

$$p(x, y, z, t = 0) = p_0 + \frac{\rho_0 V_0^2}{16} \left(\cos\left(\frac{2x}{L}\right) + \cos\left(\frac{2y}{L}\right)\right) \left(\cos\left(\frac{2z}{L}\right) + 2\right), \tag{36}$$

where the characteristic length scale is set to $L = 1$ and the subscript zero denotes constant values. The velocity scale $V_0 = M_0 c_0$ depends on the initial Mach number and the speed of sound $c_0 = \sqrt{\gamma R T_0}$ at the temperature $T_0 = \frac{p_0}{R\rho_0} = 1$. The pressure $p_0 = \frac{\rho_0 V_0^2}{\gamma M_0^2}$ and the initial density $\rho_0 = 1$ are evaluated from the state equation $\rho = \frac{p}{RT}$

with $T(x, y, z, t = 0) = T_0$. For the following simulations, the specific heat ratio is set to $\gamma = 1.4$ and the Prandtl number $Pr = 0.71$. The Reynolds number is defined as $Re = \frac{\rho_0 V_0 L}{\mu_0}$, and the dynamic viscosity is assumed to follow Sutherland's law [56]:

$$\mu(T) = \mu_0 \left(\frac{T}{T_0}\right)^{3/2} \frac{T_0 + S}{T + S}, \tag{37}$$

where $S = 0.4042$ is Sutherland's constant. To conclude the non-dimensional description of the problem, the characteristic convective time is defined as $t_c = L/V_0$, and all simulations are performed from $t_0 = 0$ to $t_f = 20t_c$ with a fixed time step of $\Delta t = 3 \times 10^{-4} t_c$ using the RK(4,4) scheme. This corresponds to a CFL ~ 0.15 for the highest spatial resolution. Different grid resolutions at a polynomial order p = 3 have been used to assess the convergence of the methods, as summarized in Table 5. The results are compared to a reference solution obtained from a pseudo-spectral method with 512^3 Fourier modes [2] for the incompressible case. For the compressible case, the reference solution comes from a simulation based on sixth-order TENO scheme performed with 2048^3 DOF [55].

Elements	Numerical DOF
16^3	64^3
32^3	128^3
64^3	256^3
128^3	512^3

Table 5: Grid resolutions for the 3D Taylor-Green vortex at $Re = 1600$ and $M_0 = 1.25$ with p = 3.

4.2.2. Numerical stability

At a Mach number $M_0 = 1.25$, the dilatational contribution to the viscous dissipation rate is large due to the presence of shock waves reaching a peak Mach number of 2 at $t/t_c = 6$ [27]. As a result, the DG method is unstable at coarse resolutions, whereas all stabilization methods maintain stability across all grid resolutions, as shown in Table 6. The proportion of troubled cells detected by both methods decreases from approximately 37% at the coarsest resolution to around 6.5% at 128^3 degrees of freedom, and drops below 1% at the finest resolution.

	32^3	64^3	128^3	256^3	512^3
DG	✗	✗	✗	✓	✓
DG-AV	✓	✓	✓	✓	✓
DG-ES	✓	✓	✓	✓	✓
ESDG-GL	✓	✓	✓	✓	✓
ESDG-GLL	✓	✓	✓	✓	✓

Table 6: Numerical stability of the methods on different grid resolutions for the 3D Taylor-Green vortex at $Re = 1600$ and $M_0 = 1.25$ with p = 3 at the fixed time step $\Delta t = 3 \times 10^{-4} t_c$. ✓: stable; ✗: unstable.

Table 7 reports the maximum stable time step for each method. At the coarsest resolution, the DG-AV and ESDG-GLL methods exhibit a less restrictive time step constraint than the methods based on the entropy projection. However, as the grid is refined, all methods demonstrate a parabolic time step restriction to be stable due to the importance of the viscous effects.

	64^3	128^3	256^3	512^3
DG	/	/	0.25	0.15
DG-AV	0.51	0.27	0.25	0.15
DG-ES	0.23	0.27	0.25	0.15
ESDG-GL	0.23	0.27	0.25	0.15
ESDG-GLL	0.51	0.54	0.31	0.19

Table 7: Maximum stable CFL of the methods on different grid resolutions for the 3D Taylor-Green vortex at $Re = 1600$ and $M_0 = 1.25$ with $\mathrm{p} = 3$.

4.2.3. Numerical results

Figure 7 presents the temporal evolution of the solenoidal contributions to the viscous dissipation rate for the 3D Taylor–Green vortex at $Re = 1600$ and $M_0 = 1.25$, using $\mathrm{p} = 3$. All methods converge to the reference solution at the finest resolution. The DG-ES and DG-AV methods consistently exhibit the highest levels of solenoidal dissipation across all grid resolutions, closely matching the performance of the vanilla DG method at the two finest resolutions. In contrast, the ESDG-GL method underpredicts the dissipation rate from the peak onward, relative to the DG-ES method, highlighting the influence of shocklets and the associated numerical error introduced by the entropy projection. The ESDG-GLL method tends to be more dissipative than ESDG-GL, further illustrating the impact of lower quadrature accuracy on the resolution of turbulent scales. The influence of numerical dissipation on small turbulent structures is depicted in Figure 8, which presents Q-criterion iso-contours colored by the z-component of the vorticity at $t/t_c = 12.5$. This time corresponds to the peak of solenoidal dissipation shown in Figure 7, using a grid resolution of 128^3 DOF. The DG-ES method (left) demonstrates superior performance in capturing small turbulent structures due to its low level of dissipation compared to the ESDG-GLL method (right). Accurately resolving these small-scale structures, even under conditions of under-resolution and the presence of shocklets, is essential for predicting the correct flow enstrophy and, consequently, the solenoidal dissipation rate in more complex flow configurations.

Figure 9 illustrates the temporal evolution of the dilatational contribution to the viscous dissipation rate, primarily driven by dilatation effects such as strong compression waves. Numerically, the degree of dilatation is closely linked to the intensity of shocks. A high level of dilatation indicates that the method applies low numerical dissipation, enabling the capture of sharper shock profiles but at the risk of introducing spurious oscillations that may compromise the simulation's stability. Conversely, a low level of dilatation signifies high numerical dissipation, resulting in smoother, thicker shock profiles. This behavior is evident with the DG-AV method, which reduces shock intensity and consistently underpredicts the dilatational dissipation rate across all resolutions. In

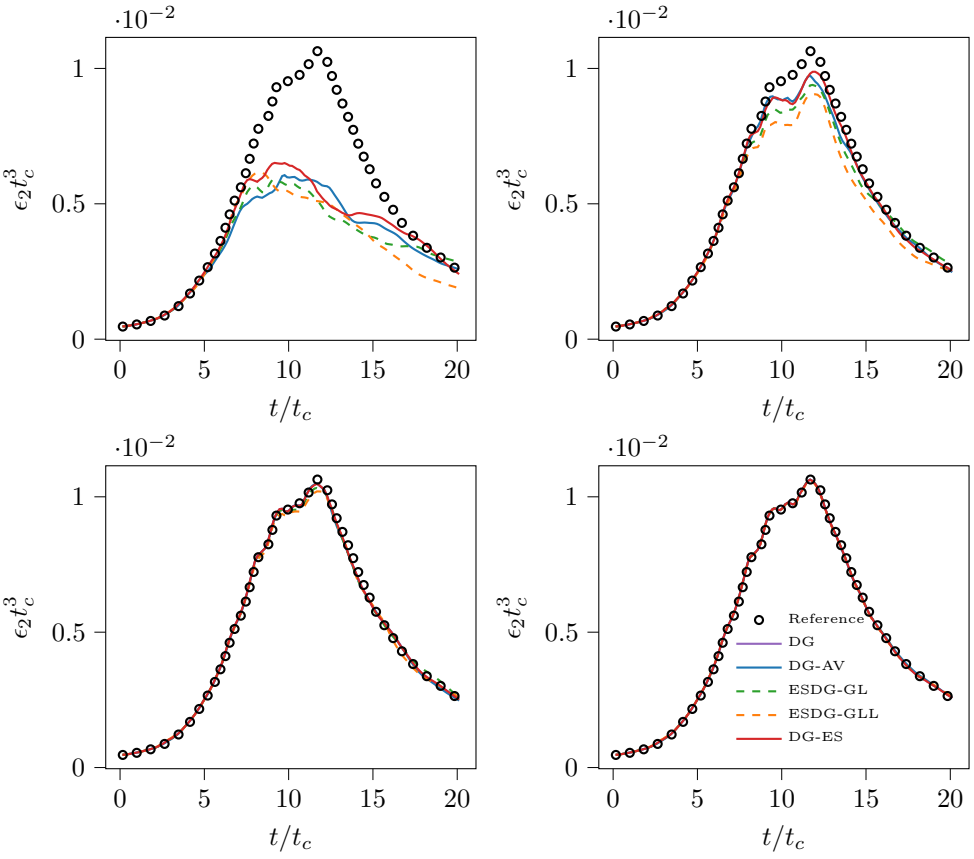

Figure 7: Temporal evolution of the solenoidal contribution to the viscous dissipation rate for the 3D Taylor-Green vortex at $Re = 1600$ and $M_0 = 1.25$ with p = 3. Top left: 64^3 DOF; top right: 128^3 DOF; bottom left: 256^3 DOF; bottom right: 512^3 DOF. The DG method is unstable at lower resolutions and is only shown at higher resolutions (256^3 and 512^3 DOF).

constrast, methods based on the SBP operator, which do not introduce numerical shock dissipation, tend to overpredict the dilatational dissipation rate. This overprediction is larger for the methods using the entropy projection, such as ESDG and DG-ES, highlighting the difficulty of the entropy projection in accurately representing the correct level of dilatation. As explained in Section 3.3, entropy variables have a larger impact on the solution at surface quadrature points, leading to larger errors in surface quantities, such as the divergence of velocity (via the divergence theorem). Interestingly, the DG-ES method does not match with the vanilla DG method, unlike for the solenoidal dissipation. At finer grid resolutions, the vanilla DG method shows strong convergence to the reference solution for the dilatational dissipation rate.

Figure 10 illustrates the impact of the stabilization method on the profiles of the Mach number at the first peak of dilatational dissipation ($t/t_c = 2.5$), extracted along a line in the y-direction at $x = z = 0$. At the coarsest resolution, all methods exhibit significant oscillations, with the DG-AV method producing a visibly thicker shock profile.

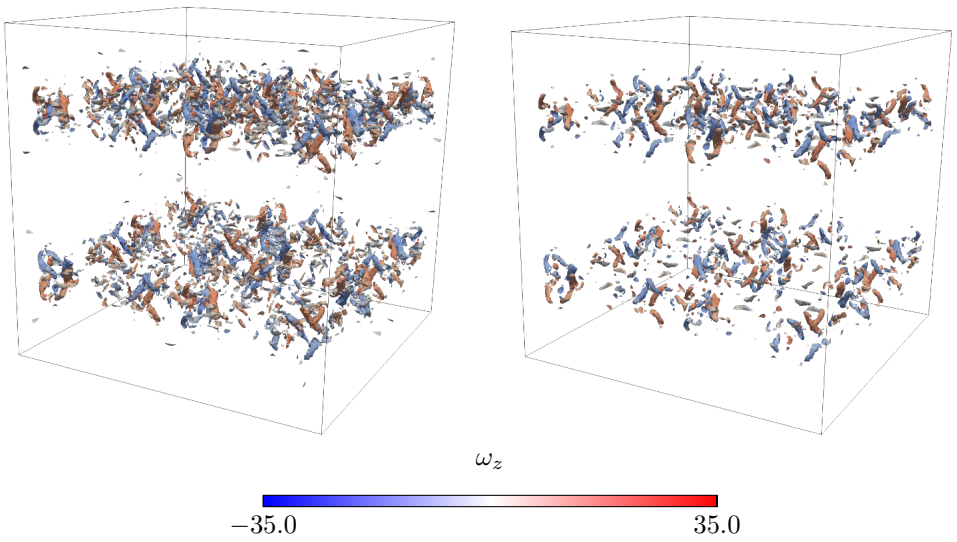

Figure 8: Q-criterion iso-surfaces colored by the z-component of the vorticity for the 3D Taylor-Green vortex at $Re = 1600$ and $M_0 = 1.25$ at $t/t_c = 12.5$ and 128^3 DOF. On the left, the DG-ES method and on the right, the ESDG-GLL method.

At 128^3 DOF, DG-AV significantly reduces oscillations compared to the entropy-based methods. In contrast, the ESDG-GL and DG-ES methods exhibit larger undershoots and overshoots near the shock, whereas the ESDG-GLL method shows better control of oscillations. At the finest resolution, all methods converge toward a sharp shock profile. DG-AV remains free of oscillations. Both ESDG-GL and DG-ES display minor undershoots at the shock, while ESDG-GLL still shows some oscillations upstream. The vanilla DG method, despite the absence of any added numerical dissipation, achieves an almost oscillation-free profile at the highest resolution.

Finally, the pressure dilatation, ϵ_4, is presented in Figure 11 for the various methods. The reference solution for this term is derived using the vanilla DG with 512^3 DOF, as no comparable data exists in the literature to the authors' knowledge. All methods demonstrates convergence toward a similar solution as the grid resolution increases. However, the ESDG-GL method introduces larger errors than other methods, particularly at the coarsest grid resolution, and exhibits slower spatial convergence. The mapping from the entropy variables to the conservative variables (12) defines the specific energy density ρe as an exponential function of the physical entropy. While the entropy is a convex function, the mapping is well-posed. Issues arise near large pressure gradients such as those caused by shock waves, under-resolved turbulent features, or near vacuum states. In such situations, the entropy can become nearly non-convex, leading to ill-conditioning of the mapping. This ill-conditioning results in significant errors in the projected variables, particularly in the pressure computed directly from the specific energy density. The novel DG-ES method addresses this issue by selectively activating the entropy projection only in regions with under-resolved features. By limiting the projection to problematic areas, the DG-ES method improves the accuracy of the pressure dilatation representation, as

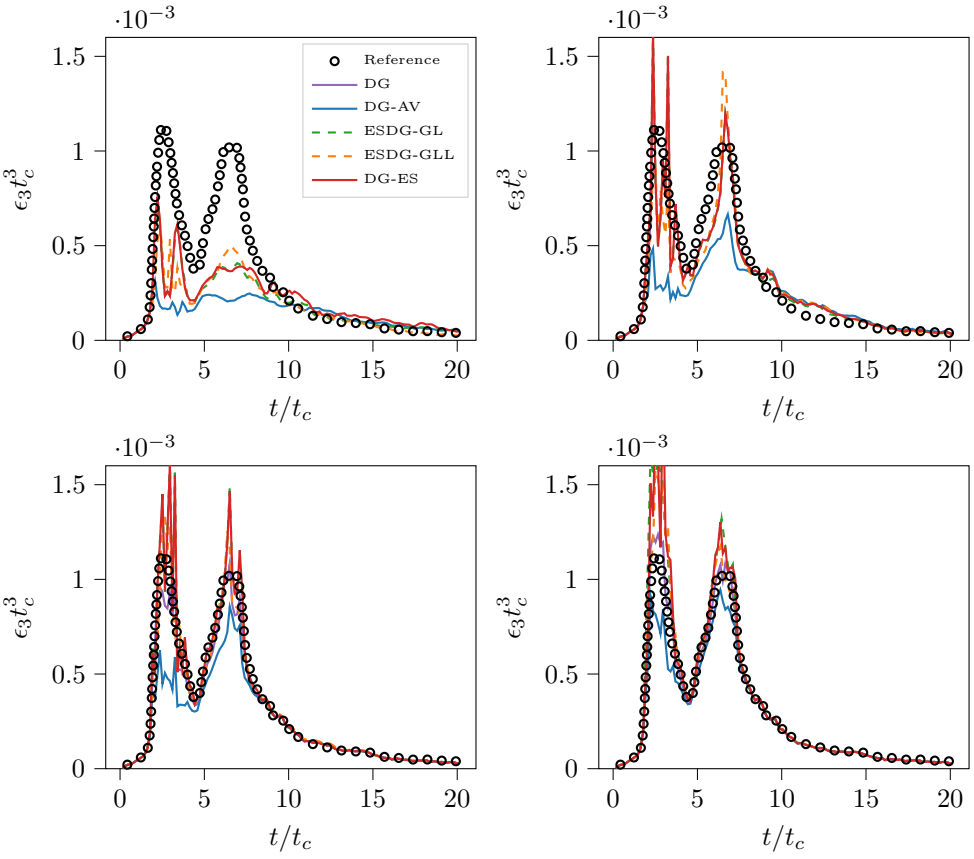

Figure 9: Temporal evolution of the dilatational contribution to the viscous dissipation rate for the 3D Taylor-Green vortex at $Re = 1600$ and $M_0 = 1.25$ with p = 3. Top left: 64^3 DOF; top right: 128^3 DOF; bottom left: 256^3 DOF; bottom right: 512^3 DOF.

observed after $t/t_C = 10$ for the coarsest grid and at any time for the other resolutions. The ESDG-GLL method exhibits a similar level of fluctuations to the DG-ES method, with larger errors at the coarsest grid resolution. The DG-AV method shows the best performance in representing the pressure dilatation at the coarsest grid resolution.

4.2.4. Computational cost

Table 8 presents the computational cost of the different methods for the 3D Taylor-Green vortex case with p = 3 and a grid of 64^3 cells. As expected, the ESDG-GL method is the most computationally expensive due to its use of SBP operators and Gauss–Legendre quadrature. The DG-ES method achieves a substantial reduction in cost compared to the fully stabilized ESDG method, though it remains more expensive than the other approaches. The cost savings from DG-ES are somewhat reduced in this case due to a higher number of troubled cells across the domain. The DG-AV method is the most efficient, with a cost increase of less than 10% relative to the vanilla DG method, while also demonstrating the best overall performance in terms of robustness

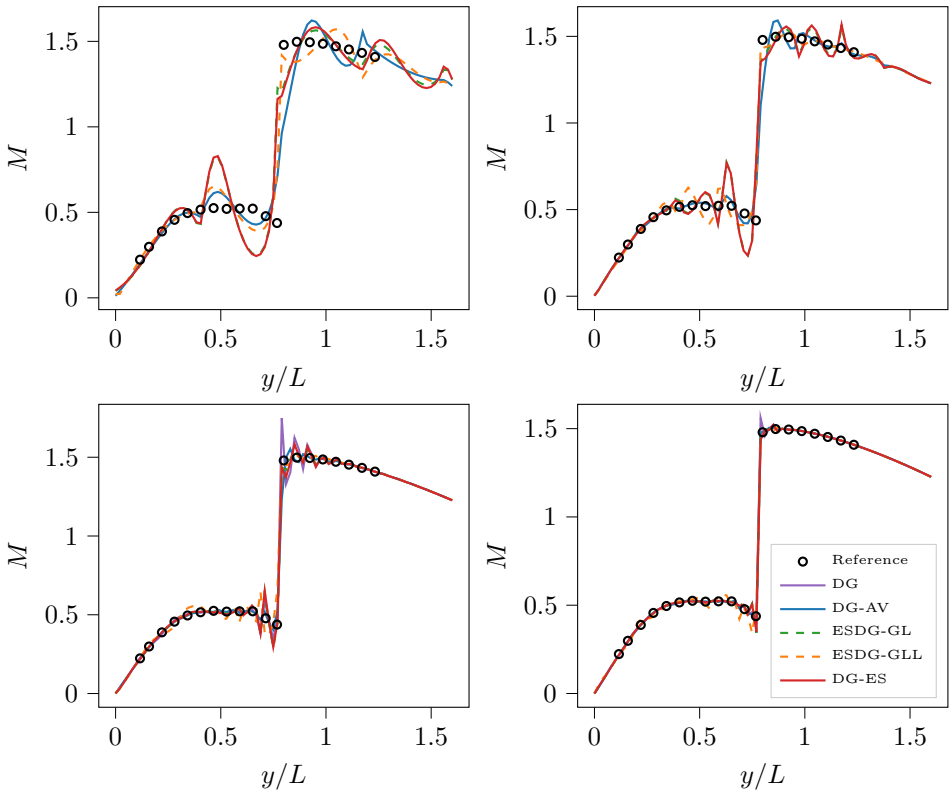

Figure 10: Profiles of the Mach number extracted from the y line at $x = y = 0$ at $t/t_c = 2.5$, for the 3D Taylor-Green vortex at $Re = 1600$ and $M_0 = 1.25$ with p = 3. Top left: 64^3 DOF; top right: 128^3 DOF; bottom left: 256^3 DOF; bottom right: 512^3 DOF.

and accuracy for this test case. The ESDG-GLL method is slightly more expensive than DG-AV but remains significantly cheaper than ESDG-GL for almost the same level of accuracy.

DG	DG-AV	DG-ES	ESDG-GL	ESDG-GLL
1	1.07	1.27	1.86	1.16

Table 8: Computational cost of the different methods normalized by the cost of the vanilla DG method for the 3D Taylor-Green vortex at $Re = 1600$, $M = 1.25$ with p = 3 and 64 cells per direction. CPU: 2x AMD EPYC 7763 64-core @2.45 GHz.

4.3. Inviscid strong-vortex/shock-wave interaction

As third test case, we consider the two-dimensional inviscid interaction between a strong vortex and a stationary shock wave [57]. Although this case is not strictly turbu-

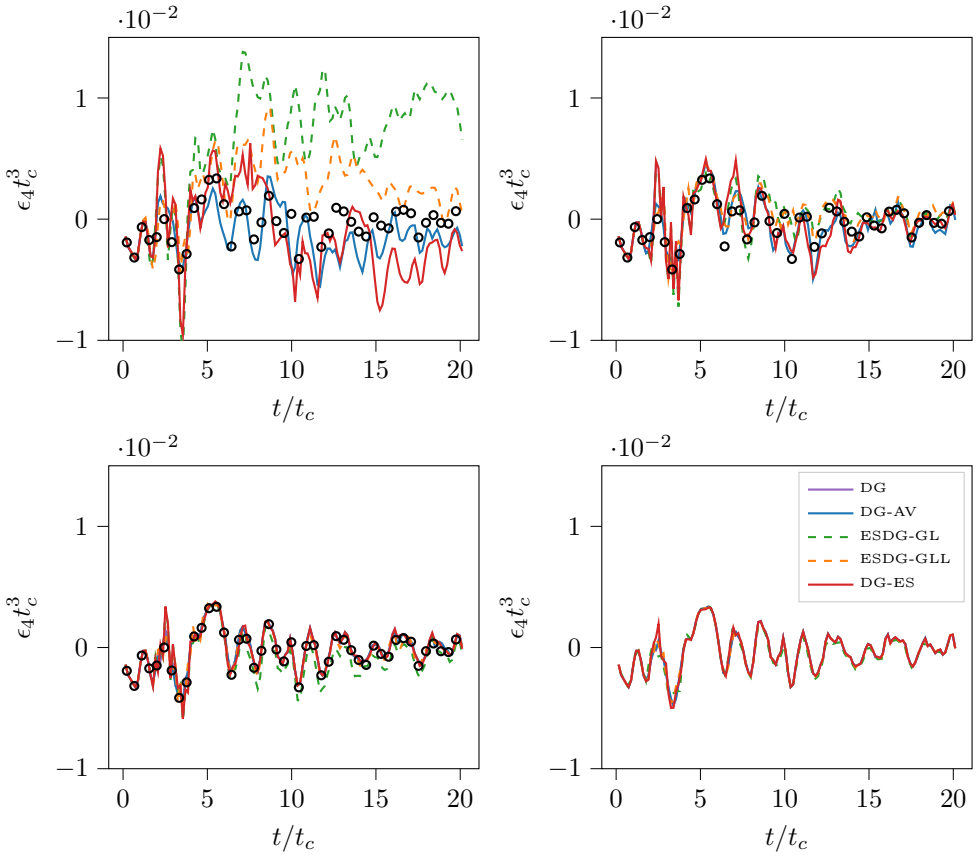

Figure 11: Temporal evolution of the pressure dilatation for the 3D Taylor-Green vortex at $Re = 1600$ and $M_0 = 1.25$ with p = 3. Top left: 64^3 DOF; top right: 128^3 DOF; bottom left: 256^3 DOF; bottom right: 512^3 DOF. The reference solution, circle symbol, is obtained from the vanilla DG method with 512^3 DOF.

lent, it provides a valuable benchmark for assessing the ability of the methods to capture both shock waves and vortex structures.

4.3.1. Case description and computational setup

The computational domain is defined as $\Omega = (0, 2) \times (0, 1)$, with a stationary normal shock wave located at $x_s = 0.5$. The inflow Mach number is set to $M_s = 1.5$, and the flow proceeds from left to right. The upstream flow conditions are specified as $(\rho_0, u_0, v_0, p_0) = \left(1, M_s\sqrt{\gamma}, 0, 1\right)$, where $\gamma = 1.4$, while the downstream conditions are determined using the Rankine–Hugoniot relations. A counter-clockwise rotating vortex is initialized within the domain, centered at $(x_v, y_v) = (0.25, 0.4)$, with semi-axes $(a, b) = (0.075, 0.175)$ and a vortex strength defined by $M_v = v_m/\sqrt{\gamma} = 0.9$. The angular velocity of the vortex is

given by

$$\boldsymbol{v}_\theta(r) = \begin{cases} v_m \dfrac{r}{a} & \text{if } r \leq a, \\ v_m \dfrac{a}{a^2 - b^2}\left(r - \dfrac{b^2}{r}\right) & \text{if } a < r \leq b, \\ 0 & \text{if } r > b, \end{cases} \tag{38}$$

where r denotes the distance from the vortex center. The remaining flow variables within the vortex are derived from the ideal gas law and the assumption of isentropic flow. The left and right boundaries are set to supersonic inlet and subsonic outlet conditions, respectively. The top and bottom boundaries are treated as slip-wall boundary. Two grid resolutions are considered: 100×50 and 200×100 elements, with a polynomial order of $\mathrm{p} = 3$. The reference solution is obtained using a high-resolution finite volume solver with approximately 18×10^6 DOF, as provided by the 5th International Workshop on High-Order CFD Methods (HiOCFD5) [58]. The RK(4,4) time integration scheme is used with a time step size of $\Delta t = 1 \times 10^{-4}$ for the coarsest grid and $\Delta t = 2.5 \times 10^{-5}$ for the finest grid, corresponding to $\mathrm{CFL} = 0.16$ and $\mathrm{CFL} = 0.08$, respectively. These values represent the maximum common CFL number that ensures stability across all methods, as further discussed in the next section. All simulations are performed over the time interval $t \in [0, 0.7]$.

4.3.2. Numerical stability

Due to the presence of a strong shock wave, the vanilla DG method becomes unstable at the considered grid resolutions, whereas the fully entropy-stable methods maintain numerical stability. However, the troubled-cell indicator α is not sufficiently robust in this case to stabilize the DG-AV and DG-ES schemes. To enhance stability, the sensor is modified by applying a single diffusion sweep

$$\alpha = \max_{\mathcal{K}} \left(\alpha, 0.5\alpha_{\mathcal{K}}\right), \tag{39}$$

where $\alpha_{\mathcal{K}}$ denotes the sensor value in all elements sharing a face. While this modification improves robustness, it also extends the region where stabilization is applied, potentially impacting solution accuracy, as discussed in the following section. The maximum proportion of troubled cells detected by the sensor is approximately 9.5% for the DG-ES method and 4% for the DG-AV method at the coarsest resolution, decreasing to about 3.5% and 1.5%, respectively, at the finest resolution.

The entropy stable methods based on the entropy projection impose stricter time step constraints, requiring significantly lower CFL numbers for stability, as shown in Table 9. Moreover, the time step constraint for the entropy stable methods based on the entropy variables decrease quadratically with grid refinement, rather than linearly as might be expected. In contrast, the DG-AV and ESDG-GLL methods maintains a stable CFL number of ~ 0.8 across resolutions.

4.3.3. Numerical results

Figure 12 shows the non-dimensional density fields for the strong vortex/shock-wave interaction problem at two key time instances: $t/t_c = 0.3$, when the vortex interacts with the shock, and $t = 0.7$, during the vortex-splitting stage, both shown at the coarsest grid resolution. At this resolution, the DG-AV method provides clean, oscillation-free

	DG-AV	DG-ES	ESDG-GL	ESDG-GLL
p = 3, 100 × 50	0.8	0.16	0.16	0.86
p = 3, 200 × 100	0.8	0.08	0.08	0.86

Table 9: Maximum stable CFL number for the different methods for the strong vortex/shock-wave interaction problem.

shock capture but significantly under-resolves the vortex structures. In contrast, DG-ES captures the vortex features more accurately but introduces visible oscillations in the shock region. These differences are further examined in Figure 13, which presents the density distribution along the line $y = 0.4$ at $t = 0.7$ for both grid resolutions and all methods. The line plots confirm the improved vortex resolution of the entropy-stable methods over DG-AV on coarse meshes, while also highlighting the oscillatory behavior near and downstream of the shock. At finer resolution, all methods converge toward the reference solution, although the entropy-stable schemes still exhibit mild oscillations just upstream of the vortex and the DG-AV method continues to underpredict the vortex density.

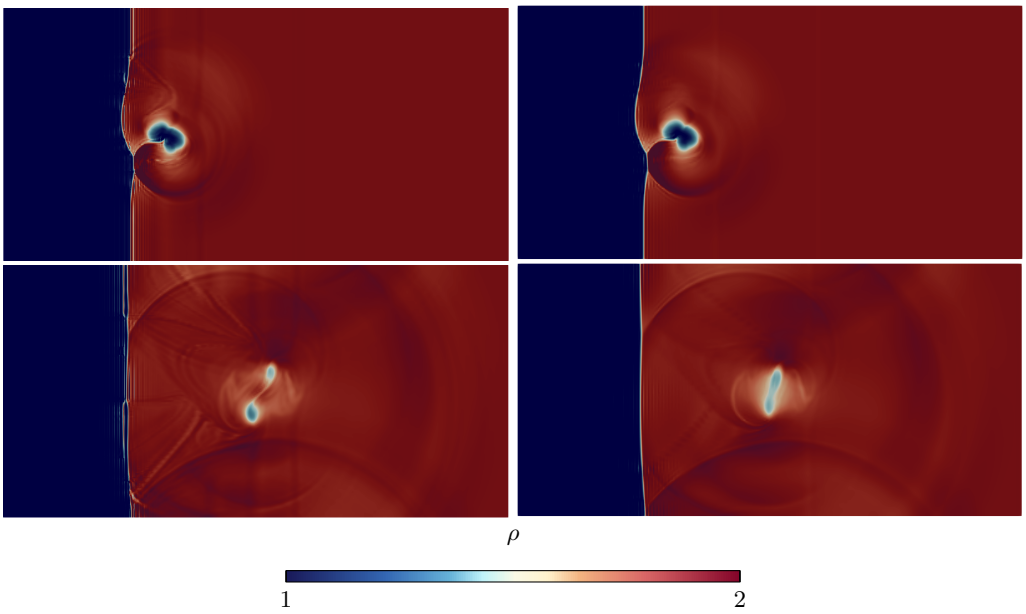

Figure 12: Non-dimensional density fields of the strong-vortex/shock-wave interaction problem with p = 3 and 100 × 50 elements at times $t = 0.3$ (top) and $t = 0.7$ (bottom). On the left, the DG-ES method is used, while on the right, the DG-AV method is employed.

Figure 14 displays the sensor fields at the same time instances as in Figure 12. These fields illustrate two key features. First, the DG-ES method exhibits significantly higher sensor activation near the shock, reflecting the sensitivity of entropy-stable schemes to shock presence. Second, in both methods and throughout the entire simulation, the

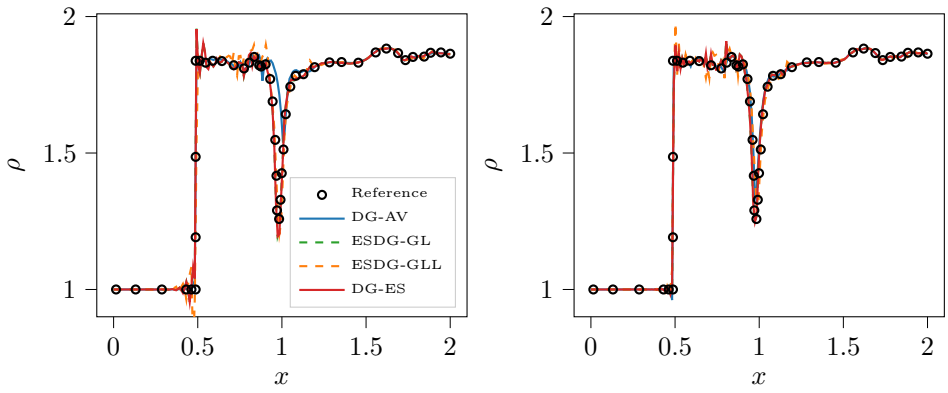

Figure 13: Distribution of density of the strong-vortex/shock-wave interaction problem along the line $y = 0.4$ at $t = 0.7$ with $\mathrm{p} = 3$ and 100×50 elements (left) and 200×100 elements (right).

sensor is not triggered in the vortex regions. This indicates that the under-resolution of vortex structures observed with the DG-AV method is not caused by artificial viscosity being applied within the vortex itself, but rather results from dissipation introduced during the earlier interaction phase between the vortex and the shock.

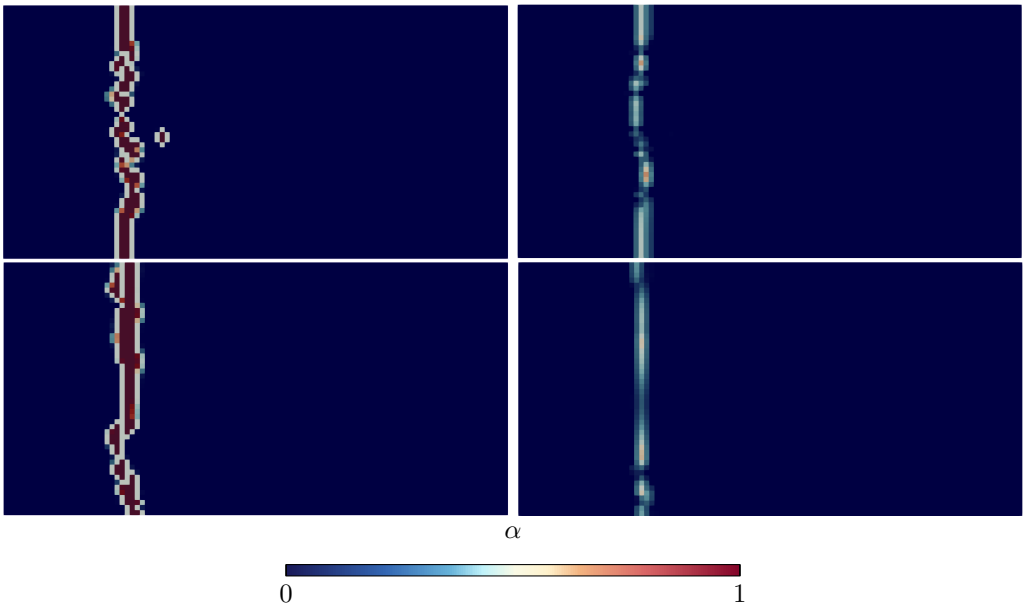

Figure 14: Snapshot of the sensor α fields of the strong-vortex/shock-wave interaction problem with $\mathrm{p} = 3$ and 100×50 elements at times $t = 0.3$ (top) and $t = 0.7$ (bottom). On the left, the DG-ES method is used, while on the right, the DG-AV method is employed.

4.3.4. Computational cost

Table 10 compares the computational cost of the different methods normalized by the cost of the DG-AV method for the strong vortex/shock-wave interaction problem. All simulations were performed using p = 3 on a 200×100 mesh.

DG-AV	DG-ES	ESDG-GL	ESDG-GLL
1	1.28	1.68	1.01

Table 10: Computational cost of the different methods normalized by the cost of the DG-AV method for the strong-vortex/shock-wave interaction problem with p = 3 and 200×100 elements. CPU: 2x AMD EPYC 7763 64-core @2.45 GHz.

4.4. Shock turbulence interaction

The final test case focuses on the well-known shock–turbulence interaction problem, which has been widely investigated in previous studies [59, 60, 61, 62]. It involves a normal shock wave interacting with upstream homogeneous isotropic turbulence. The incoming turbulence is characterized by a turbulent Mach number of $M_{t,0} = 0.22$ and a Taylor-scale Reynolds number of $Re_\lambda = 40$. This interaction causes significant changes in the flow, including the amplification of turbulence and the generation of acoustic and entropy waves.

4.4.1. Case description and computational setup

The computational domain is defined as a box with dimensions $[4\pi \times 2\pi \times 2\pi]$, where $x = x_1$ represents the streamwise direction, and $y = x_2$ and $z = x_3$, denote the transverse directions. A nearly stationary normal shock is initially positioned at $x = \pi$, in agreement with the laminar Rankine-Hugoniot relations. Periodic boundary conditions are applied in the transverse directions, while a sponge layer is implemented from $x = 3\pi$ to the downstream end of the domain. Within this zone, flow variables are gradually relaxed toward a laminar base state using a smoothing function, effectively suppressing nonphysical oscillations near the outflow, as demonstrated by Larsson and Lele [59]. A constant back pressure, derived from the Rankine–Hugoniot relations, is prescribed at the outflow boundary. This boundary treatment induces only minor fluctuations in the shock position [59]. The turbulence is considered homogeneous in the transverse directions and isotropic upstream of the shock wave. Flow statistics are obtained by averaging over the homogeneous directions and time t. The Reynolds stresses are defined as $R_{ij} = \widetilde{v_i'' v_j''}$, where Favre averages are indicated by a tilde, $\widetilde{f} = \overline{\rho f}/\overline{\rho}$ and the fluctuations are defined as $f'' = f - \widetilde{f}$.

At the domain inlet, isotropic turbulence is superimposed on a uniform mean flow with a Mach number of $M = 1.28$, and subsequently convected downstream under the assumption of Taylor's frozen turbulence hypothesis. The inflow turbulence is generated using a separate temporal simulation of decaying homogeneous isotropic turbulence, following the methodology of Ristorcelli and Blaisdell [63]. The velocity field in this precursor simulation is initialized from a three-dimensional Gaussian spectral density with zero mean velocity and a peak wave number of $\tilde{k}_M = 6$. The simulation is advanced in time

until the turbulence develops to a state characterized by a velocity derivative skewness of approximately -0.5 and a flatness factor approaching 4.0. At this stage, the resulting turbulence exhibits a turbulent Mach number $M_t = 0.22$, and a Taylor-scale Reynolds number of $Re_\lambda = 40$.

Two grid resolutions are considered: 368×64^2 and 736×128^2 DOF. The reference solution is taken from the simulation by Larsson and Lele [59]. The computational mesh is Cartesian, with no element clustering near the shock, ensuring uniform spatial resolution throughout the domain. The simulation is advanced in time using the RK(4,4) scheme with a time step of $\Delta t = 0.02/(\tilde{k}_M v_{\mathrm{rms},0})$, which corresponds to a CFL number of CFL $=$ 0.535. Statistical averaging is performed over a time interval $\Delta t_{\mathrm{stat}} = 100/(\tilde{k}_M v_{\mathrm{rms},0})$.

4.4.2. Numerical stability

As in the strong vortex–shock-wave interaction case, the vanilla DG method is unstable at the tested grid resolutions, whereas all stabilized methods remain numerically stable. At the coarsest resolution, the maximum proportion of troubled cells detected by the sensor is approximately 6% for the DG-ES method and 2% for the DG-AV method. At the finest resolution, these values decrease to around 3% and 1.5%, respectively.

Table 11 presents the maximum stable CFL numbers for each method, which remain nearly constant across mesh refinements. Due to the reduced shock strength in this case, the methods using Gauss quadrature (DG-AV, DG-ES and ESDG-GL) achieve similar CFL limits. The ESDG-GLL method, based on Gauss–Lobatto quadrature, supports a slightly higher CFL number.

DG-AV	DG-ES	ESDG-GL	ESDG-GLL
0.53	0.53	0.53	0.69

Table 11: Maximum stable CFL number for the different methods for the shock-turbulence interaction problem.

4.4.3. Numerical results

Figure 15 presents the streamwise and transverse Reynolds stress components, R_{11} and R_{22}, respectively, normalized by their values upstream of the shock, and compared against the reference solution from Larsson and Lele [59]. Both methods reproduce the expected monotonic decay of Reynolds stresses upstream of the shock and the sharp amplification of R_{11} downstream, attributed to the unsteady shock motion. At the coarsest resolution, the entropy stable methods capture more accurately the post-shock amplification of both stress components than DG-AV, without introducing spurious oscillations; further highlighting the impact of the numerical dissipation on the turbulent structures during the interaction. Upon mesh refinement, the methods exhibit convergence toward the reference solution, with diminishing differences in stress profiles.

4.4.4. Computational cost

The computational cost results are presented in Table 12. Similar to the strong vortex–shock wave interaction case, the ESDG-GLL method exhibits a computational cost comparable to that of the DG-AV method.

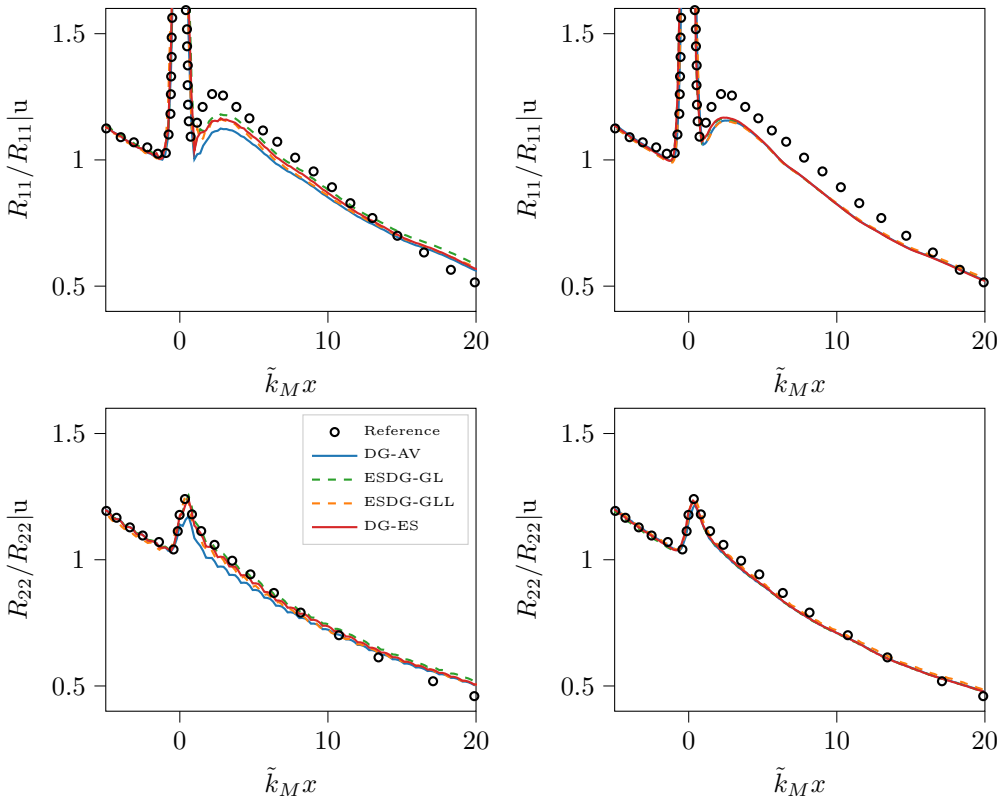

Figure 15: Streamwise (top) and transverse (bottom) Reynolds stress profiles for the shock–turbulence interaction case. Results are shown at two resolutions: 368×64^2 DOF (left) and 736×128^2 DOF (right). Reference data from Larsson and Lele [59] are included for comparison.

DG-AV	DG-ES	ESDG-GL	ESDG-GLL
1	1.21	1.58	1.06

Table 12: Computational cost of the different methods normalized by the cost of the DG-AV method for the shock-turbulence interaction problem with 736×128^2 DOF. CPU: 2x AMD EPYC 7763 64-core @2.45 GHz.

5. Conclusion

This study examines the performance of several discontinuous Galerkin Spectral Element (DG) stabilization techniques for scale-resolved simulations of compressible turbulence, with a focus on accuracy, robustness, and computational efficiency. The key contributions of this work are (1) a detailed comparison of different DG variants across a range of challenging flow conditions and (2) the introduction of the new DG-ES method, which selectively applies entropy stabilization in under-resolved regions, achieving a bal-

ance between accuracy, efficiency and robustness.

Key findings from the numerical results are summarized as follows. In terms of accuracy, the DG-AV method performs surprisingly well in cases involving highly mobile shocks, accurately capturing both shock positions and small-scale turbulent structures. However, for stationary shock configurations, it tends to alter the shock–turbulence interaction, leading to reduced accuracy in the post-shock turbulent field, even when no explicit numerical dissipation is applied in the turbulence region. In contrast, entropy-stable methods (DG-ES, ESDG-GL, and ESDG-GLL) offer a more accurate representation of post-shock turbulence but are prone to oscillations in the vicinity of shocks. In mobile shock cases, ESDG-GL and ESDG-GLL are generally more dissipative and less accurate than DG-AV and DG-ES. The ESDG-GL method is particularly affected by projection errors arising from the ill-conditioning of the entropy-to-conservative variable mapping in shock-dominated regions, which degrades the accuracy of key flow quantities, such as dilatational dissipation and pressure dilatation, and hinders kinetic energy budget closure. The ESDG-GLL method, while avoiding projection errors, suffers from under-integration due to Gauss-Lobatto quadrature, resulting in higher numerical dissipation. Regarding sensitivity to user-defined parameters, the DG-AV method is more sensitive than DG-ES, with its accuracy depending significantly on the choice of detector and, unexpectedly, on the choice of the Lagrange control points. A spectral element-type approach, where Lagrange points coincide with Gauss-Legendre quadrature points, clearly outperforms the classical formulation, in which the two sets of points are distinct. Overall, the DG-ES method delivers the most accurate representation of turbulent structures across all test cases.

In terms of robustness, all stabilization methods demonstrate spatial robustness across grid resolutions. However, methods relying on entropy variables are more sensitive to shock strength and require smaller time steps for stability. For weaker shocks, time step restrictions are similar across all methods.

In terms of computational cost, among the tested schemes, DG-AV is the most efficient, incurring less than a 10% cost increase compared to the vanilla DG method across all cases. The DG-ES method significantly reduces the cost compared to the fully entropy-stable ESDG-GL method, with a runtime comparable to ESDG-GLL depending on the number of troubled cells. All cost comparisons are made under a fixed time step shared by all methods.

These findings highlight the importance of selecting appropriate stabilization strategies for compressible turbulence, particularly in the presence of shocks. The DG-AV method is recommended when robust and efficient shock resolution is the primary concern, while the DG-ES approach is better suited for accurately capturing under-resolved turbulent structures. Recent studies propose entropy-stable methods with positivity-preserving limiters to reduce sensitivity to shocks [40, 64, 65, 66]. However, these schemes often rely on first or second order finite-volume discretizations, leading to potential accuracy degradation that requires further evaluation. As demonstrated in this work, even modest numerical dissipation introduced near shocks by DG-AV can degrade post-shock turbulence representation, despite no explicit stabilization in that region.

These conclusions are based on the specific test cases analyzed. Future work will explore these stabilization approaches in more complex flow scenarios, including shock turbulence interactions at varying turbulent Mach numbers, higher Reynolds numbers, and more realistic engineering configurations.

Acknowledgement

This research is funded by the Fonds de la Recherche Scientifique de Belgique (F.R.S.-FNRS) through a FRIA grant fellowship. The present research benefited from computational resources made available on Lucia, the Tier-1 supercomputer of the Walloon Region, infrastructure funded by the Walloon Region under the grant agreement n°1910247.

References

[1] K. Hillewaert, Development of the discontinuous Galerkin method for high-resolution, large scale CFD and acoustics in industrial geometries, Ph.D. thesis, Université Catholique de Louvain (02 2013).

[2] C. Carton de Wiart, K. Hillewaert, M. Duponcheel, G. Winckelmans, Assessment of a discontinuous Galerkin method for the simulation of vortical flows at high Reynolds number, International Journal for Numerical Methods in Fluids 74 (2013). doi:10.1002/fld.3859.

[3] S. Collis, Discontinuous Galerkin methods for turbulence simulations, in: Center for Turbulence Research, Proceedings of the Summer Program 2002, 2002.

[4] A. Uranga, P.-O. Persson, M. Drela, J. Peraire, Implicit Large Eddy Simulation of transitional flows over airfoils and wings, 2009. doi:10.2514/6.2009-4131.

[5] A. Beck, T. Bolemann, D. Flad, H. Frank, G. Gassner, F. Hindenlang, C.-D. Munz, High-order discontinuous Galerkin spectral element methods for transitional and turbulent flow simulations, International Journal for Numerical Methods in Fluids 76 (2014) n/a–n/a. doi:10.1002/fld.3943.

[6] A. Frère, K. Hillewaert, H. Sarlak, R. Mikkelsen, P. Chatelain, Cross-validation of numerical and experimental studies of transitional airfoil performance, 2015. doi:10.2514/6.2015-0499.

[7] K. Hillewaert, C. Carton de Wiart, G. Verheylewegen, T. Arts, Assessment of a high-order discontinuous Galerkin method for the direct numerical simulation of transition at low-Reynolds number in the T106C high-lift low pressure turbine cascade, 2014, p. V02BT39A034. doi:10.1115/GT2014-26739.

[8] G. Lopes, L. Simonassi, S. Lavagnoli, Impact of unsteady wakes on the secondary flows of a high-speed low-pressure turbine cascade, International Journal of Turbomachinery, Propulsion and Power 8 (4) (2023) 36. doi:10.3390/ijtpp8040036.

[9] L. Simonassi, G. Lopes, S. Lavagnoli, Effects of periodic incoming wakes on the aerodynamics of a high-speed low-pressure turbine cascade, International Journal of Turbomachinery, Propulsion and Power 8 (3) (2023) 35. doi:10.3390/ijtpp8030035.

[10] R. Hartmann, Higher-order and adaptive discontinuous Galerkin methods with shock-capturing applied to transonic turbulent delta wing flow, International Journal for Numerical Methods in Fluids 72 (8) (2013) 883–894. doi:https://doi.org/10.1002/fld.3762.

[11] E. Johnsen, J. Larsson, A. Bhagatwala, W. Cabot, P. Moin, B. Olson, P. Rawat, S. Shankar, B. Sjögreen, H. Yee, X. Zhong, S. Lele, Assessment of high-resolution methods for numerical simulations of compressible turbulence with shock waves, J. Comput. Physics 229 (2010) 1213–1237.

[12] G. Gassner, A. Beck, On the accuracy of high-order discretizations for underresolved turbulence simulations, Theoretical and Computational Fluid Dynamics 27 (06 2012). doi:10.1007/s00162-011-0253-7.

[13] L. Diosady, S. Murman, Higher-order methods for compressible turbulent flows using entropy variables, in: 53rd AIAA Aerospace Sciences Meeting, Kissimmee, Florida, 2015.

[14] K. Hillewaert, J.-S. Cagnone, S. M. Murman, A. Garai, Y. Lv, M. Ihme, Assessment of high-order DG methods for LES of compressible flows, in: Proceedings of the Center for Turbulence Research Summer Program 2016, 2016, pp. 363–372.

[15] P.-O. Persson, J. Peraire, Sub-cell shock capturing for discontinuous Galerkin methods, AIAA paper 2 (01 2006). doi:10.2514/6.2006-112.

[16] P. Fernandez, N. Nguyen, J. Peraire, A physics-based shock capturing method for large-eddy simulation, arXiv preprint arXiv:1806.06449 (June 2018). doi:10.48550/arXiv.1806.06449.

[17] G. J. Gassner, A. R. Winters, D. A. Kopriva, Split form nodal discontinuous Galerkin schemes with summation-by-parts property for the compressible Euler equations, Journal of Computational Physics (2016).

[18] J. Chan, H. Ranocha, T. Warburton, On the entropy projection and the robustness of high order entropy stable discontinuous Galerkin schemes for under-resolved flows, Frontiers in Physics (2022) 32.
[19] D. Rojas, R. Boukharfane, L. Dalcin, D. C. D. R. Fernández, H. Ranocha, D. E. Keyes, M. Parsani, On the robustness and performance of entropy stable collocated discontinuous Galerkin methods, Journal of Computational Physics 426 (2021) 109891.
[20] H. Ranocha, M. Schlottke-Lakemper, J. Chan, A. M. Rueda-Ramirez, A. R. Winters, F. Hindenlang, G. J. Gassner, Efficient implementation of modern entropy stable and kinetic energy preserving discontinuous Galerkin methods for conservation laws, ACM Transactions on Mathematical Software (2023) 30.
[21] J. Chan, D. Del Rey Fernández, M. Carpenter, Efficient entropy stable gauss collocation methods, SIAM Journal on Scientific Computing 41 (2019) A2938–A2966. doi:10.1137/18M1209234.
[22] J. Chan, On discretely entropy conservative and entropy stable discontinuous Galerkin methods, Journal of Computational Physics 362 (2018) 346–374. doi:https://doi.org/10.1016/j.jcp.2018.02.033.
[23] J. Chan, Skew-symmetric entropy stable modal discontinuous Galerkin formulations, Journal of Scientific Computing 81 (1) (2019) 459–485.
[24] D. Wang, Y. Du, Y. Jin, J. Cai, F. Liao, Comparative study on predicting turbulent kinetic energy budget using high-order upwind scheme and non-dissipative central scheme, Advances in Aerodynamics 6 (1) (2024) 24. doi:10.1186/s42774-024-00187-z.
[25] O. Zeman, Dilatation dissipation: The concept and application in modeling compressible mixing layers, Physics of Fluids 2 (2) (1990) 178–188. doi:10.1063/1.857767.
[26] S. Sarkar, G. Erlebacher, M. Y. Hussaini, H. O. Kreiss, The analysis and modelling of dilatational terms in compressible turbulence, Journal of Fluid Mechanics 227 (1991) 473–493. doi:10.1017/S0022112091000204.
[27] D. Lusher, N. Sandham, Assessment of low-dissipative shock-capturing schemes for the compressible Taylor–Green vortex, AIAA Journal 59 (August 2020). doi:10.2514/1.J059672.
[28] A. Harten, On the symmetric form of systems of conservation laws with entropy, Journal of Computational Physics 49 (1) (1983) 151–164. doi:10.1016/0021-9991(83)90118-3.
[29] T. Hughes, L. Franca, M. Mallet, A new finite element formulation for computational fluid dynamics: I. symmetric forms of the compressible Euler and Navier-Stokes equations and the second law of thermodynamics, Computer Methods in Applied Mechanics and Engineering 54 (2) (1986) 223–234.
[30] E. Tadmor, Entropy stability theory for difference approximations of nonlinear conservation laws and related time-dependent problems, Acta Numerica (2003).
[31] M. Zakerzadeh, G. May, Entropy stable discontinuous Galerkin scheme for the compressible Navier-Stokes equations, in: 55th AIAA Aerospace Sciences Meeting, 2017, aIAA 2017-0084. doi:10.2514/6.2017-0084.
[32] W. H. Reed, T. R. Hill, Triangular mesh methods for the neutron transport equation, Los Alamos Scientific Lab., N.Mex. (USA), 1973.
URL https://www.osti.gov/biblio/4491151
[33] B. Cockburn, C.-W. Shu, The runge–kutta discontinuous galerkin method for conservation laws v: Multidimensional systems, Journal of Computational Physics 141 (2) (1998) 199–224. doi:https://doi.org/10.1006/jcph.1998.5892.
[34] R. Hartmann, P. Houston, Symmetric interior penalty DG methods for the compressible Navier–Stokes equations i: Method formulation, International Journal of Numerical Analysis and Modeling (2006) 20.
[35] A. Harten, P. D. Lax, C. D. Levermore, W. J. Morokoff, Convex entropies and hyperbolicity for general Euler equations, SIAM Journal on Numerical Analysis 35 (6) (1998) 2117–2127. doi:10.1137/S0036142997316700.
[36] M. H. Carpenter, T. C. Fisher, E. J. Nielsen, S. H. Frankel, Entropy stable spectral collocation schemes for the Navier–Stokes equations: discontinuous interfaces, SIAM Journal on Scientific Computing 36 (5) (2014) B835–B867. doi:10.1137/130932199.
[37] J. Crean, J. E. Hicken, D. C. D. R. Fernández, D. W. Zingg, M. H. Carpenter, Entropy-stable summation-by-parts discretization of the Euler equations on general curved elements, Journal of Computational Physics (2018). doi:10.1016/j.jcp.2017.12.015.
[38] P. Chandrashekar, Kinetic energy preserving and entropy stable finite volume schemes for compressible Euler and Navier-Stokes equations, Communications in Computational Physics 14 (5) (2013) 1252–1286.
[39] J. Chan, D. Del Rey Fernández, M. Carpenter, Efficient entropy stable gauss collocation methods,

SIAM Journal on Scientific Computing 41 (2019) A2938–A2966. doi:10.1137/18M1209234.
[40] S. Hennemann, A. M. Rueda-Ramírez, F. J. Hindenlang, G. J. Gassner, A provably entropy stable subcell shock capturing approach for high order split form DG for the compressible Euler equations, Journal of Computational Physics 426 (2021) 109935.
[41] R. Vandenhoeck, A. Lani, Implicit high-order flux reconstruction solver for high-speed compressible flows, Computer Physics Communications 242 (2019) 1–24.
[42] J. S. Park, C. Kim, Higher-order multi-dimensional limiting strategy for discontinuous galerkin methods in compressible inviscid and viscous flows, Computers & Fluids 96 (2014) 377–396. doi:https://doi.org/10.1016/j.compfluid.2013.11.030.
[43] J. Chan, Z. Wang, A. Modave, J.-F. Remacle, T. Warburton, Gpu-accelerated discontinuous galerkin methods on hybrid meshes, Journal of Computational Physics 318 (2016) 142–168. doi:https://doi.org/10.1016/j.jcp.2016.04.003.
[44] S. Pirozzoli, F. Grasso, Direct numerical simulations of isotropic compressible turbulence: influence of compressibility on dynamics and structures, Physics of Fluids 16 (12) (2004) 4386–4407.
[45] R. Samtaney, D. I. Pullin, B. Kosović, Direct numerical simulation of decaying compressible turbulence and shocklet statistics, Physics of Fluids 13 (5) (2001) 1415–1430.
[46] S. Lele, J. Larsson, Shock-turbulence interaction: What we know and what we can learn from peta-scale simulations, Journal of Physics: Conference Series 180 (2009) 012032. doi:10.1088/1742-6596/180/1/012032.
[47] E. Johnsen, J. Larsson, A. Bhagatwala, W. Cabot, P. Moin, B. Olson, P. Rawat, S. Shankar, B. Sjögreen, H. Yee, X. Zhong, S. Lele, Assessment of high resolution methods for numerical simulations of compressible turbulence, Journal of Computational Physics 229 (2010) 1213–1237. doi:10.1016/j.jcp.2009.10.028.
[48] D. Moro, N. Nguyen, J. Peraire, Dilation-based shock capturing for high-order methods, International Journal for Numerical Methods in Fluids 82 (02 2016). doi:10.1002/fld.4223.
[49] G. I. Taylor, A. E. Green, Mechanism of the production of small eddies from large ones, Proceedings of the Royal Society of London. Series A, Mathematical and Physical Sciences 158 (1937) 499–521.
[50] J.-B. Chapelier, M. de la Llave Plata, F. Renac, Inviscid and viscous simulations of the Taylor-Green vortex flow using a modal discontinuous Galerkin approach, in: 42nd AIAA Fluid Dynamics Conference and Exhibit 2012, 2012. doi:10.2514/6.2012-3073.
[51] M. E. Brachet, D. I. Meiron, S. A. Orszag, B. G. Nickel, R. H. Morf, U. Frisch, Small-scale structure of the Taylor–Green vortex, Journal of Fluid Mechanics 130 (1983) 411–452. doi:10.1017/S0022112083001159.
[52] N. Peng, Y. Yang, Effects of the Mach number on the evolution of vortex-surface fields in compressible Taylor-Green flows, Phys. Rev. Fluids 3 (2018) 013401. doi:10.1103/PhysRevFluids.3.013401.
[53] Z. Wang, J. Zhu, L. Tian, N. Zhao, Assessment of high-order interpolation-based weighted essentially non-oscillatory schemes for compressible Taylor–Green vortex flows, Physics of Fluids 36 (11 2024). doi:10.1063/5.0236997.
[54] J. Bull, A. Jameson, Simulation of the Taylor–Green vortex using high-order flux reconstruction schemes, AIAA Journal 53 (2015) 2750–2761. doi:10.2514/1.J053766.
[55] J.-B. Chapelier, D. Lusher, W. van Noordt, C. Wenzel, T. Gibis, P. Mossier, A. Beck, G. Lodato, C. Brehm, M. Ruggeri, C. Scalo, N. Sandham, Comparison of high-order numerical methodologies for the simulation of the supersonic Taylor–Green vortex flow, Physics of Fluids 36 (05 2024). doi:10.1063/5.0206359.
[56] W. Sutherland, The viscosity of gases and molecular force, The London, Edinburgh, and Dublin Philosophical Magazine and Journal of Science 36 (223) (1893) 507–531. doi:10.1080/14786449308620508.
[57] A. Rault, G. Chiavassa, R. Donat, Shock-vortex interactions at high mach numbers, Journal of Scientific Computing 19 (2003) 347–371. doi:10.1023/A:1025316311633.
[58] H. You, C. Kim, High-order multi-dimensional limiting strategy with subcell resolution, Journal of Computational Physics 375 (09 2018). doi:10.1016/j.jcp.2018.09.011.
[59] J. Larsson, S. K. Lele, Direct numerical simulation of canonical shock/turbulence interaction, Physics of Fluids 21 (12) (2009) 126101. doi:10.1063/1.3275856.
[60] J. Larsson, I. Bermejo-Moreno, S. Lele, Reynolds- and mach-number effects in canonical shock-turbulence interaction, Journal of Fluid Mechanics 717 (2013) 293–321. doi:10.1017/jfm.2012.573.
[61] J. Ryu, D. Livescu, Turbulence structure behind the shock in canonical shock-vortical turbulence interaction, Journal of Fluid Mechanics 756 (2014) R1. doi:10.1017/jfm.2014.477.
[62] Y. Tian, F. Jaberi, Z. Li, D. Livescu, Numerical study of variable density turbulence interaction with a normal shock wave, Journal of Fluid Mechanics 829 (2017) 551–588. doi:10.1017/jfm.2017.542.

[63] J. R. Ristorcelli, G. A. Blaisdell, Consistent initial conditions for the dns of compressible turbulence, Physics of Fluids 9 (1) (1997) 4–6.

[64] N. Krais, A. Beck, T. Bolemann, H. Frank, D. Flad, G. Gassner, F. Hindenlang, M. Hoffmann, T. Kuhn, M. Sonntag, C.-D. Munz, Flexi: A high order discontinuous galerkin framework for hyperbolic–parabolic conservation laws, Computers & Mathematics with Applications 81 (2021) 186–219. doi:https://doi.org/10.1016/j.camwa.2020.05.004.

[65] Y. Lin, J. Chan, I. Tomas, A positivity preserving strategy for entropy stable discontinuous galerkin discretizations of the compressible euler and navier-stokes equations, Journal of Computational Physics 475 (2022) 111850. doi:10.1016/j.jcp.2022.111850.

[66] A. Mateo-Gabín, A. M. Rueda-Ramírez, E. Valero, G. Rubio, A flux-differencing formulation with gauss nodes, Journal of Computational Physics 489 (2023) 112298. doi:https://doi.org/10.1016/j.jcp.2023.112298.